











Uranium Abundances and Ages of *R*-process Enhanced Stars with Novel U II Lines*

SHIVANI P. SHAH ¹, RANA EZZEDDINE ¹, ALEXANDER P. JI ^{2,3}, TERESE HANSEN ⁴, IAN U. ROEDERER ^{5,6},
MÁRCIO CATELAN ^{7,8,9}, ZOE HACKSHAW ¹⁰, ERIKA M. HOLMBECK ^{11,12}, TIMOTHY C. BEERS ^{13,6} AND
REBECCA SURMAN ^{13,6}

¹Department of Astronomy, University of Florida, 211 Bryant Space Science Center, Gainesville, FL 32601, USA

²Department of Astronomy & Astrophysics, University of Chicago, 5640 S Ellis Avenue, Chicago IL 60637, USA

³Kavli Institute for Cosmological Physics, University of Chicago, Chicago IL 60637, USA

⁴Department of Astronomy, Stockholm University, AlbaNova University Centre, SE-106 91 Stockholm, Sweden

⁵Department of Astronomy, University of Michigan, 1085 S. University Ave., Ann Arbor, MI 48109, USA

⁶Joint Institute for Nuclear Astrophysics – Center for the Evolution of the Elements (JINA-CEE), USA

⁷Instituto de Astrofísica, Facultad de Física, Pontificia Universidad Católica de Chile, Av. Vicuña Mackenna 4860, 7820436 Macul, Santiago, Chile

⁸Millennium Institute of Astrophysics, Nuncio Monseñor Sotero Sanz 100, Of. 104, 7500000 Providencia, Santiago, Chile

⁹Centro de Astroingeniería, Facultad de Física, Pontificia Universidad Católica de Chile, Av. Vicuña Mackenna 4860, 7820436 Macul, Santiago, Chile

¹⁰Department of Astronomy, University of Texas at Austin, 2515 Speedway, Austin, Texas 78712-1205, USA

¹¹The Observatories of the Carnegie Institution for Science, 813 Santa Barbara St, Pasadena, CA 91101, USA

¹²Hubble Fellow

¹³Department of Physics and Astronomy, University of Notre Dame, Notre Dame, IN 46556, USA

ABSTRACT

The ages of the oldest stars shed light on the birth, chemical enrichment, and chemical evolution of the Universe. Nucleocosmochronometry provides an avenue to determining the ages of these stars independent from stellar evolution models. The uranium abundance, which can be determined for metal-poor *r*-process enhanced (RPE) stars, has been known to constitute one of the most robust chronometers known. So far, U abundance determination has used a *single* U II line at $\lambda 3859$ Å. Consequently, U abundance has been reliably determined for only five RPE stars. Here, we present the first homogeneous U abundance analysis of four RPE stars using two novel U II lines at $\lambda 4050$ Å and $\lambda 4090$ Å, in addition to the canonical $\lambda 3859$ Å line. We find that the U II lines at $\lambda 4050$ Å and $\lambda 4090$ Å are reliable and render U abundances in agreement with the $\lambda 3859$ U abundance, for all the stars. We, thus, determine revised U abundances for RPE stars, 2MASS J09544277+5246414, RAVE J203843.2–002333, HE 1523–0901, and CS 31082–001, using multiple U II lines. We also provide nucleocosmochronometric ages of these stars based on the newly derived U, Th, and Eu abundances. The results of this study open up a new avenue to reliably and homogeneously determine U abundance for a significantly larger number of RPE stars. This will, in turn, enable robust constraints on the nucleocosmochronometric ages of RPE stars, which can be applied to understand the chemical enrichment and evolution in the early Universe, especially of *r*-process elements.

1. INTRODUCTION

Ages of the oldest stars aid our understanding of chemical enrichment and evolution in the early universe, the assembly history of our Galaxy (e.g., Marín-Franch et al. 2009; Bonaca et al. 2020; Xiang & Rix 2022; Rix et al. 2022; Buder et al. 2022), and the age of the Universe (e.g., Bond et al. 2013; VandenBerg et al. 2014; Jimenez et al. 2019; Valcin et al. 2020; Abdalla et al. 2022). Most techniques used to infer stellar ages, including isochrone placement and asteroseismology, depend on a detailed understanding of low-metallicity stellar-evolution mod-

* Some of the data presented herein were obtained at the W. M. Keck Observatory, which is operated as a scientific partnership among the California Institute of Technology, the University of California and the National Aeronautics and Space Administration. The Observatory was made possible by the generous financial support of the W. M. Keck Foundation. Additionally, this work is based on observations made with ESO Telescopes at the La Silla Paranal Observatory under programme IDs 275.D-5028(A), 077.D-0453(A), and 165.N-0276(A). This paper also includes data gathered with the 6.5 meter Magellan Telescopes located at Las Campanas Observatory, Chile.

els, which is challenging and still evolving (e.g., Miglio et al. 2013; Epstein et al. 2014; Joyce & Chaboyer 2015; Tayar et al. 2017; Catelan 2018; Valentini et al. 2019). On the other hand, nucleocosmochronometry, a radioactive-dating technique, offers an independent avenue to determining the ages of some of the oldest stars (Soderblom 2010; Catelan 2018).

Nucleocosmochronometry uses the decay of long-lived actinides, uranium (^{238}U ; $\tau_{1/2} = 4.47$ Gyr) and thorium (^{232}Th ; $\tau_{1/2} = 14.05$ Gyr), to estimate the ages of metal-poor stars (Francois et al. 1993; Cowan et al. 1991; Cayrel et al. 2001; Frebel & Kratz 2009). U and Th are created solely via the rapid-neutron capture process (*r*-process) (Burbidge et al. 1957; Cameron 1957). Therefore, *r*-process-enhanced (RPE) stars, classified as having $[\text{Eu}/\text{Fe}] > +0.3^1$ (Beers & Christlieb 2005; Holmbeck et al. 2020), have been some of the best candidates for employing nucleocosmochronometry (Frebel 2018). RPE stars are typically metal-poor ($[\text{Fe}/\text{H}] \lesssim -1.5$; Frebel (2018)), offering the ability to detect the weak absorption lines of U and Th in their spectra. Moreover, the *r*-process enrichment of RPE stars is the result of only a few *r*-process nucleosynthetic events, dismissing the need for galactic chemical enrichment models in nucleocosmochronometry (Frebel 2018; Arnould & Goriely 2020). In practice, the absolute ages of the stars are determined by using the observed present-day abundance ratios and theoretical production ratios (PRs) of U and/or Th to coproduced *r*-process elements e.g., U/Th, U/X, and Th/X, where X refers to a lighter stable *r*-process element, such as Eu, Os, and Ir (e.g., Cowan et al. 1997, 1999; Cayrel et al. 2001; Hill et al. 2002; Frebel et al. 2007; Placco et al. 2017).

One of the major systematic uncertainties in nucleocosmochronometry is the PRs of Th and U to lighter *r*-process elements like Eu (Goriely & Arnould 2001; Schatz et al. 2002). This issue has been prominently highlighted by the negative Th/Eu stellar ages obtained for 30% of RPE stars, termed as actinide-boost stars (Roederer et al. 2009; Mashonkina et al. 2014; Holmbeck et al. 2018). The negative stellar ages are a result of the observed Th/Eu abundance ratios being higher than the Th/Eu PRs predicted by current *r*-process models. More generally, the application of the Th/Eu chronometer to RPE stars has led to a large range in ages from 21 Gyr to -9 Gyr, even though these stars are metal-poor (Ji & Frebel 2018; Holmbeck et al. 2018). These anomalies have indicated that the astrophysical conditions of

r-process nucleosynthetic events may be varying event-to-event, with the PRs of actinides to lighter *r*-process elements sensitive to these changes. Consequently, no one set of Th/X and U/X PR may be applicable to all RPE stars (Holmbeck et al. 2019a).

On the other hand, the U/Th chronometer results in high-fidelity stellar-age estimates even for the actinide-boost stars (Cayrel et al. 2001; Hill et al. 2002; Frebel et al. 2007; Placco et al. 2017; Holmbeck et al. 2018). Since U and Th have similar nuclear masses and are synthesized along similar reaction channels during the *r*-process, their PR is robust to major shortcomings of *r*-process models (Arnould & Takahashi 1999; Goriely & Clerbaux 1999; Schatz et al. 2002). Additionally, any variations in the *r*-process astrophysical conditions are expected to impact the actinides, U and Th, equally, so that their PR is generally constant across all *r*-process nucleosynthetic events (e.g., Holmbeck et al. 2019a), with the uncertainty in the predicted value of the PR largely due to the unknown nuclear data of the neutron-rich actinides (Holmbeck et al. 2019b; Lund et al. 2022).

However, it is particularly challenging to reliably determine U abundance. So far, in the context of nucleocosmochronometry, U abundance has been confidently determined for only five highly *r*-process enhanced ($[\text{Eu}/\text{Fe}] > +0.7$) stars: namely CS 31082-001 (Cayrel et al. 2001; Hill et al. 2002), HE 1523-0901 (Frebel et al. 2007), 2MASS J09544277+5246414 (Holmbeck et al. 2018), RAVE J203843.2-002333 (Placco et al. 2017), and CS 29497-004 (Hill et al. 2017). Canonically, and also in the case of these five stars, a *single* U II line at $\lambda 3859 \text{ \AA}$ has been used to determine the U abundance of RPE stars. This line is blended with the wing of a strong Fe I line and a poorly-constrained CN feature, rendering a reliable U abundance determination challenging. Moreover, the proximity to the CN feature limits the study of U in stars with strong C enhancements. Interestingly, the U abundance of the Przybylski star (HD 101065), a chemically peculiar star, has been determined using 17 U II transitions (Shulyak et al. 2010).

In this study, we have homogeneously determined the U abundance of four highly RPE stars using two novel U II lines at $\lambda 4050$ and $\lambda 4090 \text{ \AA}$, in addition to the canonical $\lambda 3859 \text{ \AA}$ line. We revisit the U abundances of 2MASS J09544277+5246414 (hereafter J0954+5246), RAVE J203843.2-002333 (hereafter J2038-0023), HE 1523-0901, and CS 31082-001 to investigate the utility of the two new U II lines. This work is aimed at serving as a benchmark test for the reliable determination of U abundances and subsequently stellar ages of RPE stars using multiple U II lines, in an effort to advance the field of nucleocosmochronometry.

¹ $[A/B] = \log(N_A/N_B)_{\text{Star}} - \log(N_A/N_B)_{\text{Solar}}$, where N is the number density of the element.

Hereafter, this paper is organized as follows: Section 2 describes the observations and data reduction of the stars. Section 3 discusses their atmospheric stellar-parameter estimates. The chemical-abundance analysis of the pertinent elements, including U, Th, and Eu, is described in section 4. In Section 5, we present the nucleocosmochronometric ages of the stars using the newly derived U, Th, and Eu abundances. Finally, in section 6, we discuss our results and in section 7, we present the main conclusions of this work.

2. DATA ACQUISITION AND REDUCTION

A robust abundance analysis of U requires high signal-to-noise (S/N) and high-resolution spectral data, since U II transition lines are weak and surrounded by blends. We obtained new spectroscopic data for J0954+5246 and J2038-0023 using high-resolution spectrographs, Keck/HIRES and Magellan/MIKE, respectively. For HE 1523-0901 and CS 31082-001, we utilized VLT/UVES archival data.

Following the data reduction and radial-velocity correction, orders of each exposure were normalized using a natural cubic spline function with sigma clipping and the strong lines masked. The normalized orders were co-added and then stitched² to furnish the final spectrum of each star. We summarize the spectral data properties of all the stars in Table 1, including the wavelength range, resolving power, and S/N per pixel of the final spectra.

2.1. 2MASS J09544277+5246414

We observed J0954+5246 with Keck/HIRESr (Vogt et al. 1994) on 2021 March 26 for a total of 6.6h. The observations were broken down as 8 exposures of 1800s, 1 exposure of 1400s, and 1 exposure of 1350s. The observations were taken with the red cross-disperser, using the $5.0 \times 0''.40$ slit and with 1×1 binning, which yielded a resolving power of $R \sim 86,600$. We used the blue and the green CCD chip data, which we reduced with MAKEE³ using standard settings. The full wavelength range of the spectra was 3600-6800 Å. We corrected each spectrum for radial velocity by cross-correlating against a high-resolution spectrum of HD 122563. We normalized, co-added, and stitched the spectra to furnish the final spectrum with S/N per pixel of 185 at 4050 Å.

2.2. RAVE J203843.2-002333

We observed J2038-0023 with Magellan/MIKE (Bernstein et al. 2003) on 2018 July 8, 2018 July 24, 2018 September 26, and 2018 November 11, for a total of 15.6h. We used the $0''.35$ slit and 2×1 binning, which yielded a resolving power of $R \sim 83,000$. Data for this star already existed (Placco et al. 2017), but with 2×2 binning, which could have undersampled the profiles of the U II lines, so we reobserved the star. We reduced the spectra from each night, together, using CarPy (Kelson et al. 2000; Kelson 2003) and corrected the radial velocity by cross-correlating against a high-resolution spectrum of HD 122563. We normalized, coadded, and stitched the spectra to furnish the final spectrum with S/N per pixel of 175 at 4050 Å.

2.3. HE 1523-0901

We used the data from Frebel et al. (2007), who observed the star with VLT/UVES (Dekker et al. 2000) in 2005 and 2006, using image slicer No. 2 and $0''.45$ slit width to achieve a resolving power of $R \sim 75,000$. The data are publicly available on the ESO raw data archive⁴. We used the BLUE 437 nm setting observations from 2006 April 22, 2006 April 23, and 2006 May 19, which amounted to a total exposure time of 3.0h. The wavelength range of the final spectrum was 3758-4990 Å, which included all the lines of interest. We reduced the data using ESOREflex (Freudling et al. 2013), with order extraction set to the recommended linear method for data collected with an image slicer. We corrected the radial velocity of each exposure by cross-correlating with a high quality MIKE/Magellan spectrum of HE 1523-0901. We normalized, co-added, and stitched the spectra to furnish the final spectrum with S/N per pixel of 200 at 4050 Å.

2.4. CS 31082-001

We used data from Hill et al. (2002), who observed the star with VLT/UVES (Dekker et al. 2000) in 2000 using $0''.45$ slit-width. The data are publicly available on the ESO raw data archive. We used the BLUE arm 380-510 nm setting observations from 2000 October 17 and 2000 October 19, which totaled 2h of exposure. The resulting resolving power was $R \sim 75,000$. We reduced the data using ESOREflex (Freudling et al. 2013), with order extraction set to the recommended optimal method. We corrected the radial velocity of each exposure by cross-correlating to a high-quality MIKE/Magellan spectrum of HE 1523-0901. We nor-

² <https://github.com/alexji/alexmods/blob/master/alexmods/specutils/continuum.py>

³ <https://sites.astro.caltech.edu/~tb/makee/>

⁴ http://archive.eso.org/eso/eso_archive_main.html

Table 1. Spectral Data Properties

Star Name	Telescope/ Instrument	Wavelength Range (Å)	Slit Width	Resolving Power ($\Delta\lambda/\lambda$)	Total Exposure (h)	S/N pix ⁻¹ at 4050 Å
2MASS J09544277+5246414	Keck/HIRESb	3600-6800	0.40''	86,600	6.6	200
RAVE J203843.2-002333	Magellan/MIKE	3200-9900	0.35''	83,000	15.6	175
HE 1523-0901	VLT/UVES	3758-4990	0.45''	75,000	3.0	200
CS 31082-001	VLT/UVES	3800-5100	0.45''	70,000	2.0	125

malized, co-added, and stitched the spectra to furnish the final spectrum with S/N of 125 per pixel at 4050 Å.

3. STELLAR PARAMETERS

We derived the stellar parameters of all the stars spectroscopically. For this purpose, we used **SMHr**⁵, the next generation spectroscopic analysis software of **SMH** (Casey 2014). **SMHr** wraps the radiative transfer code, **MOOG** (Snedden 1973) and allows the employment of various grid model atmospheres. We used **MOOG** with the proper treatment of scattering included⁶ (Sobeck et al. 2011) and employed the **ATLAS9** grid of 1D plane-parallel model atmospheres computed under the assumption of local thermodynamic equilibrium (LTE) (Castelli & Kurucz 2003).

We used equivalent widths (EWs) of Fe I and Fe II lines for stellar parameter determination of all the stars. We measured the EWs within **SMHr** by fitting Gaussian or Voigt profiles. We obtained the effective temperature (T_{eff}) by inducing equilibrium in the Fe I line-abundances with respect to the excitation potential of the lines, the surface gravity ($\log g$) by minimizing the difference between the mean Fe I and Fe II abundances, and the microturbulent velocity (ξ) by inducing an equilibrium in Fe I line-abundances with respect to the reduced EW of the lines. We solved for the stellar parameters, T_{eff} , $\log g$, and ξ , simultaneously with multiple iterations and corrected the resulting best-fit T_{eff} to the photometric scale described in Frebel et al. (2013). Subsequently, we re-derived $\log g$ and ξ as described above for T_{eff} fixed to this corrected value. We list the resulting stellar parameters of J0954+5246, J2038-0023, HE 1523-0901, and CS 31082-001 in Table 2.

The stellar parameters derived in this work agree with those determined previously in the literature within uncertainties for all the stars in our sample, except for J2038-0023. The primary disagreement for J2038-0023 is in $\log g$, where we derived $\log g = 0.57$, whereas Placco et al. (2017) derived $\log g = 1.20$ using the EW technique. Upon further investigation into this discrepancy, we suspect that it mostly originates from different implementations of scattering in **MOOG**. For homogeneity with the other stars in our sample, we adopt our derived stellar parameters for J2038-0023.

4. CHEMICAL-ABUNDANCE ANALYSIS

We derived chemical abundances for all the stars using EWs and spectral synthesis in **SMHr**. Though abundances for these stars have been previously reported in the literature, we re-derived abundances of the relevant elements for a homogeneous and consistent analysis. This enabled us to robustly constrain the transitions directly blended with the U II lines, as well as those neighboring the U II lines, which could affect the local continuum placement. We derived abundances of most light elements, including Na, Mg, Al, Si, Ca, Ti, Cr, Fe, and Zn, using the EW method. We derived abundances of the remaining light elements and the neutron-capture (n-cap) elements, including C, N, V, Mn, Sr, Y, Zr, Ba, La, Ce, Pr, Nd, Sm, Eu, Gd, Dy, Tm, Er, Th, and U, with spectral synthesis of ± 5 Å regions around the transition lines. For the abundance determination of the light and n-cap elements, we used a subset of the transition list compiled by Roederer et al. (2018). For abundance analysis with spectral synthesis, we generated the atomic-parameters linelists with **linemake**⁷ (Placco et al. 2021), which included the transition wavelengths (λ), excitation potentials (χ), oscillator strengths ($\log gf$), and hyperfine structure of the

⁵ We used <https://github.com/eholmbeck/smhr-rpa/tree/refactor-scatterplot> forked from <https://github.com/andycasey/smhr/tree/refactor-scatterplot>

⁶ <https://github.com/alexji/moog17scat>

⁷ <https://github.com/vmplacco/linemake>

Table 2. Stellar Parameters

Star	Source	T_{eff} (K)	$\log g$ (cgs)	[Fe/H]	ξ (km s ⁻¹)
J0954+5246	This work	4410 \pm 150	0.61 \pm 0.30	-2.96 \pm 0.14	2.74 \pm 0.20
	Holmbeck et al. (2018)	4340 \pm 125	0.41 \pm 0.20	-2.99 \pm 0.10	2.28 \pm 0.20
J2038-0023	This work	4519 \pm 150	0.57 \pm 0.30	-3.12 \pm 0.12	2.26 \pm 0.20
	Placco et al. (2017)	4630 \pm 100	1.20 \pm 0.20	-2.91 \pm 0.10	2.15 \pm 0.20
HE 1523-0901	This work	4607 \pm 150	0.94 \pm 0.30	-2.98 \pm 0.14	2.65 \pm 0.20
	Frebel et al. (2007)	4630 \pm 40	1.00 \pm 0.30	-2.95 \pm 0.2	2.60 \pm 0.30
CS 31082-001	This work	4793 \pm 150	1.36 \pm 0.30	-2.94 \pm 0.11	1.68 \pm 0.20
	Hill et al. (2002)	4825 \pm 120	1.50 \pm 0.30	-2.9 \pm 0.13	1.80 \pm 0.20

Table 3. Abundances and Isotopic Ratios of U II Line Blends

	Source	J0954+5246 ^a	J2038-0023 ^b	HE 1523-0901 ^c	CS 31082-001 ^d
$\log \epsilon(\text{Fe})$	This Work	4.55 \pm 0.15	4.41 \pm 0.12	4.53 \pm 0.14	4.58 \pm 0.11
	Other	4.51 \pm 0.12	4.59 \pm 0.12	4.50 \pm 0.20	4.60 \pm 0.13
$\log \epsilon(\text{C})$	This Work	4.97 \pm 0.20	5.11 \pm 0.20	5.17 \pm 0.20	5.75 \pm 0.20
	Other	4.94 \pm 0.20	5.08 \pm 0.20	5.14	5.82 \pm 0.05
¹² C/ ¹³ C	This Work	4.0	4.6	3.5	19.0
	Other	\sim 3-4	> 20.0
$\log \epsilon(\text{N})$	This Work	5.82 \pm 0.20	5.56 \pm 0.20	5.88 \pm 0.20	...
	Other	5.43	<5.22
$\log \epsilon(\text{La})$	This Work	-1.06 \pm 0.09	-1.06 \pm 0.05	-0.47 \pm 0.11	-0.65 \pm 0.07
	Other	-1.15 \pm 0.10	-0.76 \pm 0.07	-0.63	-0.60 \pm 0.04

NOTE—Source of other work: ^aHolmbeck et al. (2018), ^bPlacco et al. (2017), ^cFrebel et al. (2007), ^dHill et al. (2002).

transition lines. We used the updated atomic parameters of CH transitions from Masseron et al. (2014)⁸ and r -process isotopic ratios from Sneden et al. (2008) for the spectral synthesis of Ba, Eu, Nd, Sm, Yb, and Pb. We further detail the abundance determination of the U II line blends, U, Th, and Eu in sections 4.1, 4.2, 4.3,

and 4.4, respectively. We describe uncertainty analysis of the derived abundances in section 4.5.

⁸ <https://github.com/alexji/linemake>

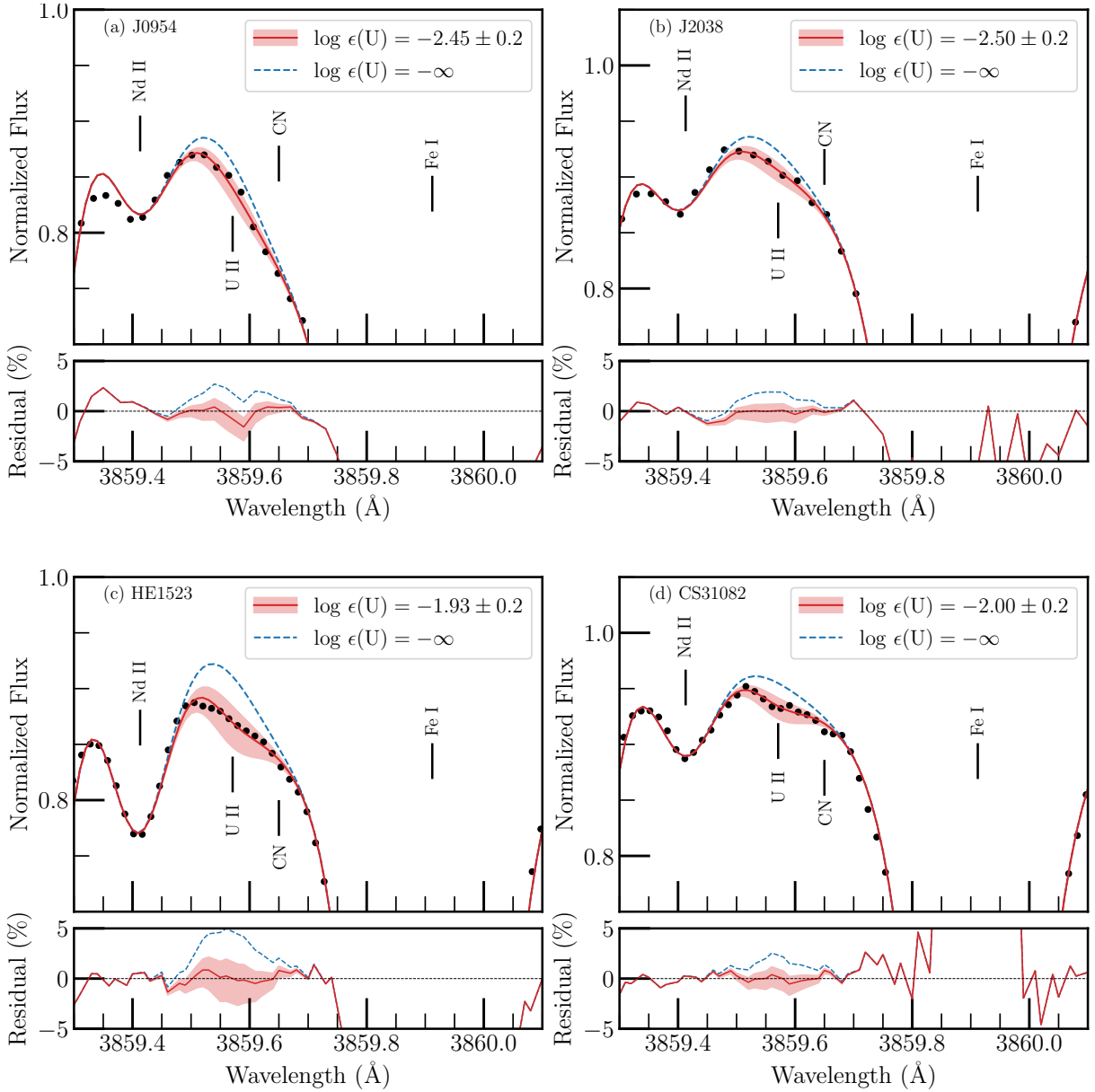


Figure 1. Spectral synthesis of the U II line at $\lambda 3859.57 \text{ \AA}$ for J0954+5246, J2038-0023, HE 1523-0901, and CS 31082-001. The red-solid line traces the best-fit synthetic model to the observed data in black points. The red-shaded region depicts abundance variation within ± 0.2 dex of the best-fit U abundance. The blue-dashed line traces the synthetic model with no U. Important neighboring transition lines are labeled. The corresponding residuals between the observed data and the synthetic models are also shown.

4.1. Blends: Fe, C, N, and La

We took special care to constrain the abundances of elements that have transitions blended with the weak U II lines. We identified that transitions of Fe I, CH, CN, and La II are blended with the U II lines investigated in this work. We obtained the Fe abundance using EW measurements of a subset of acceptable Fe I lines listed in Roederer et al. (2018), for each sample star. We estimated the uncertainty on the mean Fe abundance as the standard deviation in the abundances of the chosen

Fe I lines. We determined the C abundance by fitting the $\lambda 4313 \text{ \AA}$ G-band of CH. Based on the quality of the data and the synthetic spectrum fits, we set a fiducial uncertainty estimate of ± 0.2 dex on the C abundance of all the sample stars. With the C abundance fixed, we determined the isotopic ratio of $^{12}\text{C}/^{13}\text{C}$ by fitting the ^{13}CH feature at $\lambda 4217 \text{ \AA}$. We determined the N abundance by fitting the $\lambda 3876 \text{ \AA}$ CN molecular band for all our sample stars, except for CS 31082-001, for which we could not derive a reliable N abundance. For the

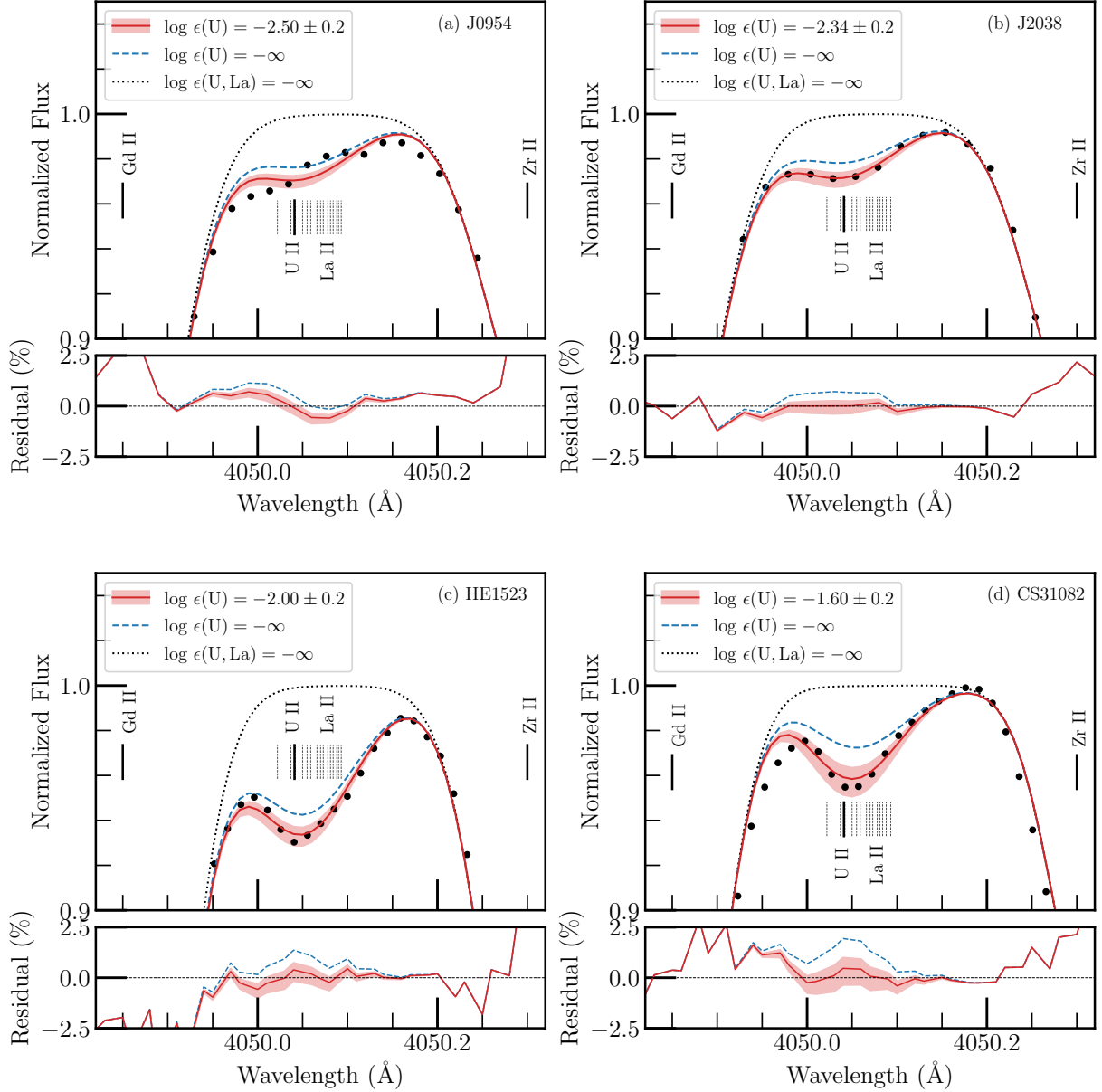


Figure 2. Spectral synthesis of the U II line at $\lambda 4050.04 \text{ \AA}$ for J0954+5246, J2038-0023, HE 1523-0901, and CS 31082-001. The red-solid line traces the best-fit synthetic model to the observed data in black points. The red-shaded region depicts the abundance variation within ± 0.2 dex of the best-fit U abundance. The blue-dashed line traces the synthetic model with no U, and the black-dotted line traces the synthetic model with no U and no La. Important neighboring transition lines are labeled. The corresponding residuals between the observed data and synthetic models are also shown.

N abundance of J0954+5246, RAVE J203843.2-002333, and HE 1523-0901, we estimated an uncertainty of ± 0.2 dex, based on the spectral synthesis fits. For each sample star, we determined the La abundance with the spectral synthesis of a subset of blend-free and acceptable La II transitions listed in Roederer et al. (2018). We estimated the uncertainty on the mean La abundance as the standard deviation in the La abundances of the chosen La II lines. We list the Fe, C, N, and La abundances and the $^{12}\text{C}/^{13}\text{C}$ isotopic ratio, determined for each star,

in Table 3, along with their corresponding values from previous literature studies. The abundances determined in this work are in agreement with the values from the literature, within uncertainties. The exception to this case is our derived La abundance for J2038-0023, which disagrees with the abundance derived by Placco et al. (2017). However, this discrepancy is simply attributed to the difference in our adopted stellar parameters (see section 3).

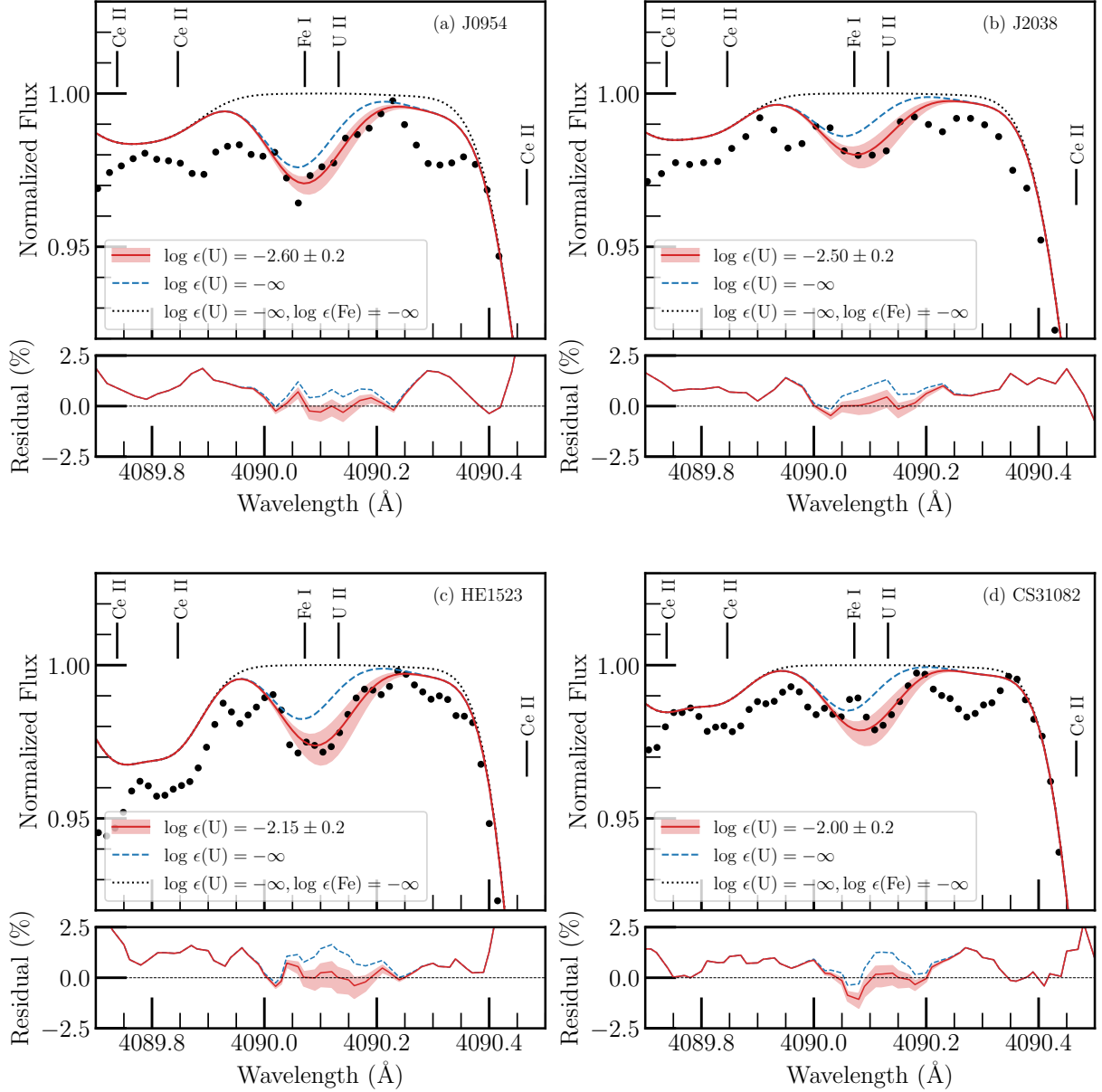


Figure 3. Spectral synthesis of the U II line at $\lambda 4090.13 \text{ \AA}$ for J0954+5246, J2038-0023, HE 1523-0901, and CS 31082-001. The red-solid line traces the best-fit synthetic model to the observed data in black points. The red-shaded region depicts the abundance variation within ± 0.2 dex of the best-fit U abundance. The blue-dashed line traces the synthetic model with no U, and the black-dotted line traces the synthetic model with no U and no Fe. Important neighboring transition lines are labeled. The corresponding residuals between the synthetic models and the observed data are also shown.

4.2. Uranium

So far in the literature, U abundances of RPE stars have been primarily determined using a single U II line at $\lambda 3859 \text{ \AA}$ ⁹. Moreover, U abundance analyses have been carried out by different studies for individual stars, with

each study varying in the employed method and atomic data.

In this study, we performed, for the first time, a homogeneous analysis to determine U abundances of four highly RPE stars using three U II lines at $\lambda 3859 \text{ \AA}$, $\lambda 4050 \text{ \AA}$, and $\lambda 4090 \text{ \AA}$. We generated the linelist for the spectral synthesis of the U II line-regions with `linemake`. We used the $\log gf$ measurements of the U II lines from Nilsson et al. (2002a), who measured them with high accuracy by combining their branching fraction calcula-

⁹ An exception to this case is Roederer et al. (2018), who also used the U II line at $\lambda 4241 \text{ \AA}$ to place an upper limit on the U abundance of an RPE star, HD 222925.

Table 4. Atomic Parameters of U II Transition Lines.

Species	λ (Å)	χ (eV)	$\log gf$	% Uncertainty in gf
U II	3859.57	0.036	-0.067	12
U II	4050.04	0.000	-0.706	7
U II	4090.13	0.217	-0.184	13

NOTE— $\log gf$ values and % uncertainty on gf values taken from Table 2 of Nilsson et al. (2002a). Excitation potential taken from linemake.

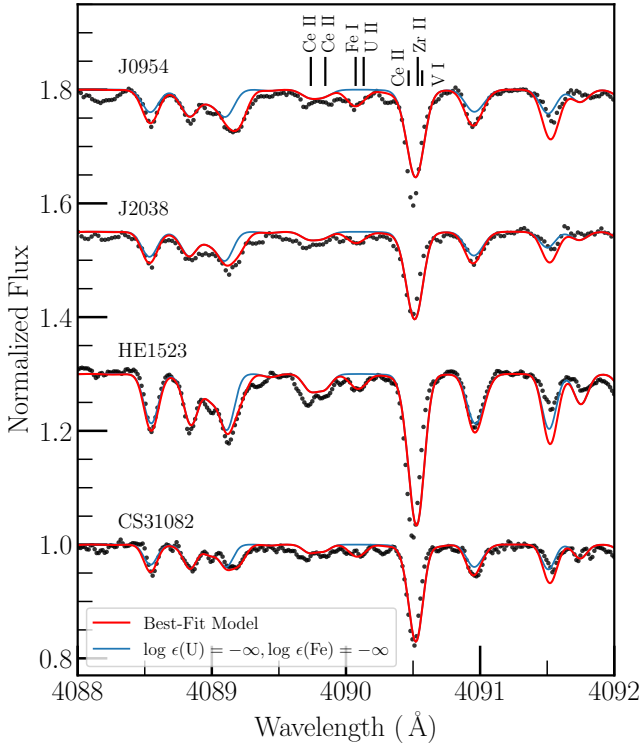


Figure 4. Spectral synthesis around the $\lambda 4090.13$ Å U II line region for J0954+5246, J2038-0023, HE 1523-0901, and CS 31082-001. The normalized flux of the stars are scaled for illustration. The red-solid line traces the best-fit synthetic model to the observed data in black points. The blue-solid line traces the synthetic model with no U and no Fe, depicting the continuum at the U II transition. Important neighboring transition lines are labeled. This zoomed-out plot depicts the best placement of the local continuum of the spectral synthesis models for our sample stars.

tions with the radiative lifetime measurements of 6 U II levels from Lundberg et al. (2001). We list the atomic parameters employed for the three U II transitions in Table 4.

We determined the final U abundance of each star as the weighted-average of the U abundances from the three U II lines i.e., $\log \epsilon(\text{U}) = \sum_i (w_i \log \epsilon_i) / \sum_i w_i$, where $\log \epsilon_i$ is the U abundance from line i and $w_i = 1/\Delta(\text{stat})_i^2$ for line i (Ji et al. 2019; McWilliam et al. 1995). We detail the method we used to estimate $\Delta(\text{stat})_i$, the statistical uncertainty on $\log \epsilon_i$, in Section 4.5. For the total uncertainty on the average-weighted U abundances, we accounted for systematic uncertainties (from stellar parameters and blends) and statistical uncertainties (from $\log gf$ measurement and continuum placement). We discuss this further in Section 4.5. We list the final weighted-average U abundance with the associated total uncertainty for all the sample stars in Table 5.

4.2.1. The $\lambda 3859$ Å U II Line

While the $\lambda 3859.57$ Å line is the strongest U II line discernible in the spectra of stars, blends from other transitions makes its spectral synthesis quite difficult. This line is situated in the wing of a strong Fe I line at $\lambda 3859.91$ Å and is further blended with a CN feature at $\lambda 3859.65$ Å, which also resides in the wing of the Fe I line. Therefore, it is essential to constrain the wing of the Fe I line as well as the CN feature for a reliable U abundance determination.

To fit the wings of the strong Fe I line, we used the Unsöld approximation (Unsöld 1955) multiplied by a factor of -8.77 for the Van der Waals hydrogen collision-damping coefficient of the Fe I line, for all the sample stars. Furthermore, we adjusted the derived Fe I abundances of the stars by -0.15 , -0.05 , $+0.02$, and $+0.03$ dex for J0954+5246, J2038-0023, HE 1523-0901, and CS 31082-001, respectively. For most of the stars, the adjustment made to the derived Fe I abundance of the star is small and lies within the uncertainty on the Fe I abundance.

To fit the CN feature, we adjusted the derived N abundance of the stars by $+0.0$, $+0.04$, and $+0.12$ dex for J0954+5246, J2038-0023, and HE 1523-0901, respectively. We find these adjustments acceptable, since they are within the ± 0.2 dex uncertainty on the derived N abundances. For CS 31082-001, we used $\log \epsilon(\text{N}) = 5.22$, which is the upper limit placed on the N abundance by Hill et al. (2002), as we could not derive a reliable N abundance for the star. We used the derived C abundance of the stars without any adjustments.

For the purpose of a better fit to the neighboring line features, we blue-shifted the transition wavelength of Nd II line at 3859.42 Å and Fe I line at 3859.21 Å by 0.07 Å. To fit the Nd II line, we adjusted the derived Nd II abundance of the star by -0.12 , $+0.0$, $+0.04$,

and -0.05 dex for J0954+5246, J2038-0023, HE 1523-0901, and CS 31082-001, respectively. The adjustment is small for most stars and within the uncertainty of the Nd abundance.

We determined $\log \epsilon(\text{U})_{3859} = -2.45, -2.50, -1.93$, and -2.0 for J0954+5246, J2038-0023, HE 1523-0901, and CS 31082-001, respectively. In Figure 1, we show the resulting best-fit spectral synthesis model for the observed data of each star, along with the residuals between the model and the data. We also depict the ± 0.2 dex abundance variation from the derived $\lambda 3859$ U abundance in red-shaded region, for all the sample stars.

4.2.2. The $\lambda 4050$ Å U II

The $\lambda 4050.04$ Å U II line is blended with a La II line at $\lambda 4050.07$ Å, which needs to be constrained well for U abundance determination. `linemake` obtains $\log gf = 0.11$ for the La II line from Corliss & Bozman (1962), but we used an updated $\log gf = 0.428$, as measured by Bord et al. (1996). We substantiated this choice with spectral synthesis of the La II line in RPE stars with minimal U contamination, which showed that the Bord et al. (1996) value provides a better fit to the observed spectra of these stars. Additionally, we blue-shifted the transition wavelength of the La II line by 0.02 Å to enable a better fit to the observed data. We also account for the hyperfine splitting (HFS) structure of this La II line, as described in Appendix A. We applied the described prescription for the La II line uniformly across all the sample stars to determine their U abundances. We employed the derived La abundance of each star in the spectral synthesis without any adjustment.

We determined $\log \epsilon(\text{U})_{4050} = -2.50, -2.34, -2.00$, and -1.60 for J0954+5246, J2038-0023, HE 1523-0901, and CS 31082-001, respectively. We show the corresponding best-fit spectral synthesis models for all the stars in Figure 2, along with the resulting residuals between the model and the observed data. We also depict ± 0.2 dex variations in the $\lambda 4050$ U abundance with a red-shaded region for all the stars. We generally find a good fit to the $\lambda 4050$ Å spectral region, as seen in Figure 2. We note an over-estimation of the synthetic model flux around $\lambda 4049.95$ Å for J0954+5246 and CS 31082-001. This could possibly indicate an unidentified line between the Gd II and U II lines that has manifested itself more strongly in J0954+5246 and CS 31082-001, as compared to in J2038-0023 and HE 1523-0901. Alternatively, the abundance of the La II HFS structure may not be well represented by the mean La abundances determined for the stars.

4.2.3. The $\lambda 4090$ Å U II line

The $\lambda 4090.13$ Å U II line is blended with one weak Fe I line at $\lambda 4090.07$ Å. We derived the $\lambda 4090$ U abundance of all the sample stars with spectral synthesis, specifically, by fitting the U II line to the red-ward wing of the Fe-U absorption feature. We determined $\log \epsilon(\text{U})_{4090} = -2.60, -2.50, -2.15$, and -2.00 for J0954+5246, J2038-0023, HE 1523-0901, and CS 31082-001, respectively. We show the corresponding best-fit spectral synthesis models for all the stars in Figure 3, along with residuals between the models and the observed data. We also depict ± 0.2 variation in the best-fit $\lambda 4050$ U abundance with red-shaded region for all the sample stars. We note that the two absorption features blue-ward and red-ward of the U II line are currently unidentified in the `linemake` linelist. We tested the effect of these unidentified features by adding “fabricated” lines to mimic them and found that they have minimal-to-no effect on the U abundance determination. In Figure 4, we also show the best-fit spectral synthesis for a wider wavelength window of this line region, for all the stars. This figure depicts that even though the immediately neighboring lines of the $\lambda 4090.13$ Å U II line are unidentified, we found an optimal continuum placement for all the stars using other spectral regions.

4.3. Thorium

We determined Th abundances for all of the sample stars using Th II lines at $\lambda 4019.13$ Å, $\lambda 4086.52$ Å, and $\lambda 4094.75$ Å. We generated the linelists for spectral synthesis with `linemake`, using $\log gf$ values from Nilsson et al. (2002b).

The Th II line at $\lambda 4019.13$ Å is the strongest Th line detectable in the optical spectra of stars. It is blended with a Ce II line at $\lambda 4019.06$ Å, a Fe I line at $\lambda 4019.04$ Å and ^{13}CH lines at $\lambda 4018.98$ Å and $\lambda 4019.15$ Å (see Figure 5). For the spectral synthesis of this region, we employed the abundances of the blends without any adjustments. We determined $\log \epsilon(\text{Th})_{4019} = -1.92, -1.70, -1.22$, and -1.18 for J0954+5246, J2038-0023, HE 1523-0901, and CS 31082-001, respectively. The corresponding best-fit spectral synthesis model is shown in Figure 5 for each star, along with the residual between the model and the observed data. We note that the synthetic spectrum is overestimated around the $\lambda 4018.98$ Å and $\lambda 4019.25$ Å regions for all the sample stars. This suggests a need to revisit the atomic parameters of the lines in this spectral region and perhaps identify unknown transitions. Nevertheless, we expect minimal effect of these wing-features on the Th abun-

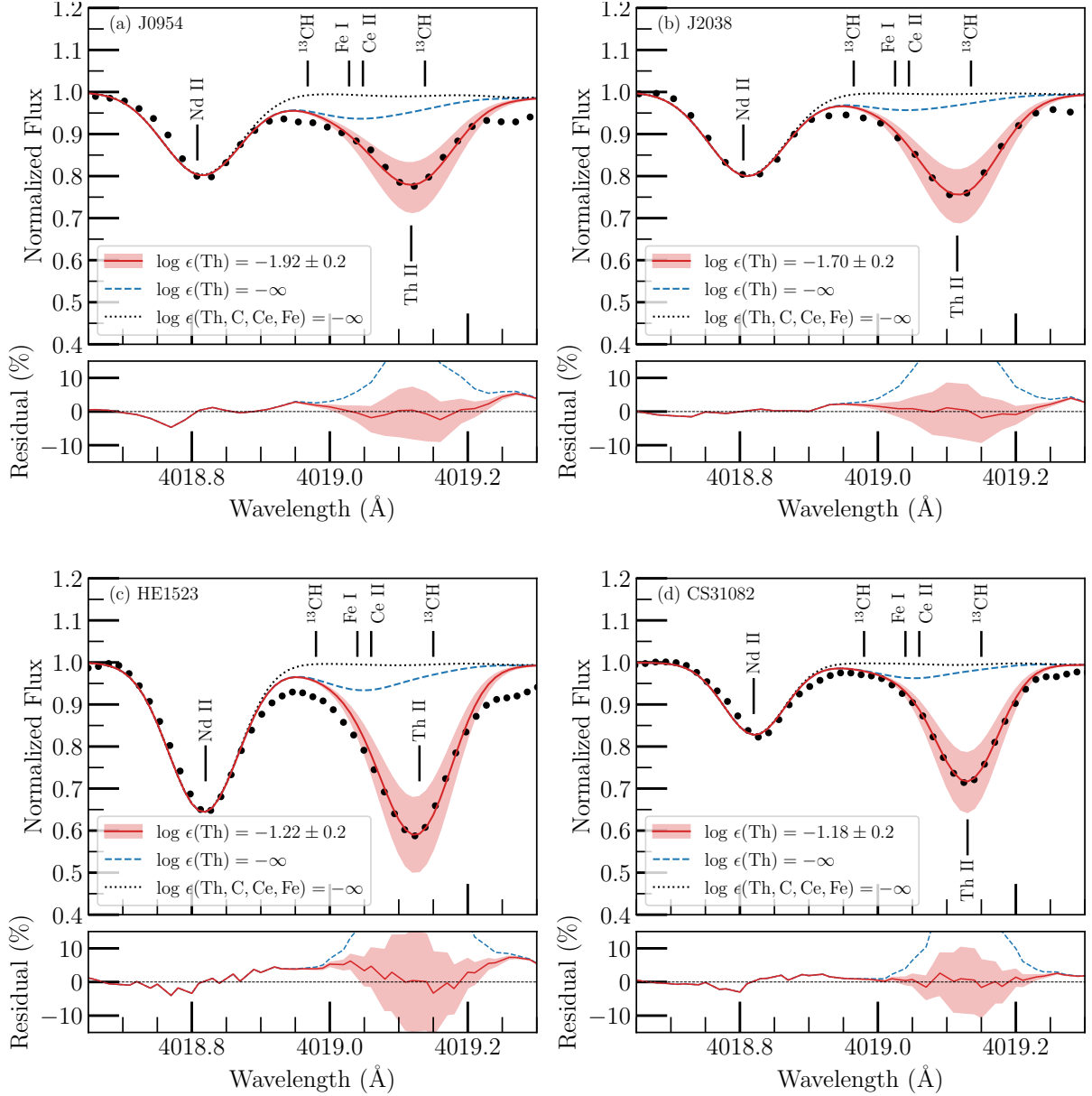


Figure 5. Spectral synthesis of the Th II line at $\lambda 4019.13 \text{ \AA}$ for J0954+5246, J2038-0023, HE 1523-0901, and CS 31082-001. The red-solid line traces the best-fit synthetic model to the observed data in black points. The blue-dashed line traces the synthetic model with no Th, and the black-dotted line traces the synthetic model with no Th, Fe, C, and Ce. The red-shaded region depicts abundance variations within ± 0.2 dex. Important neighboring transition lines are labeled. The corresponding residuals between the synthetic models and the observed data are also shown.

dance, which was robustly determined by constraining the fit of the synthetic spectrum to the core of the absorption feature.

The Th II line at $\lambda 4086.52 \text{ \AA}$ is situated next to a La II line and partly blended with a Ce II line. With spectral synthesis of this line-region, we determined $\log \epsilon(\text{Th})_{4086} = -1.70, -1.63, -0.95$, and -1.09 for J0954+5246, J2038-0023, HE 1523-0901, and CS 31082-001. For the spectral synthesis of CS 31082-001,

we adjusted the derived Ce abundance of the star by -0.05 dex.

The Th II line at $\lambda 4094.75 \text{ \AA}$ is blended with a CH line and partly blended with an Er II line. For the purpose of a good spectral synthesis fit to the region, we allowed an adjustment of the Er abundance within ± 0.2 dex of the derived Er stellar abundance for all of the sample stars. Since the Er II line is blended with only a section of the blue-ward wing of the Th II line, any adjustment of the Er abundance had minimal ef-

Table 5. U, Th, and Eu Abundances and Nucleocosmochronometric Ages.*

Source	$\log \epsilon(X)$	J0954+5246 ^a	J2038-0023 ^b	HE 1523-0901 ^c	CS 31082-001 ^d
Other Work	$\log \epsilon(U)_{3859}$	-2.13 ± 0.20	-2.14 ± 0.20	-2.06 ± 0.12	-1.92 ± 0.17
This Work	$\log \epsilon(U)_{3859}$	-2.45 ± 0.30	-2.50 ± 0.26	-1.93 ± 0.18	-2.00 ± 0.22
	$\log \epsilon(U)_{4050}$	-2.50 ± 0.33	-2.34 ± 0.30	-2.00 ± 0.48	-1.60 ± 0.21
	$\log \epsilon(U)_{4090}$	-2.60 ± 0.30	-2.50 ± 0.24	-2.15 ± 0.28	-2.00 ± 0.25
	$\log \epsilon(U)$	-2.50 ± 0.29	-2.47 ± 0.21	-1.96 ± 0.25	-1.87 ± 0.19
Other Work	$\log \epsilon(Th)$	-1.13 ± 0.10	-1.24 ± 0.10	-1.2 ± 0.05	-0.98 ± 0.13
This Work	$\log \epsilon(Th)_{4019}$	-1.92 ± 0.09	-1.70 ± 0.05	-1.22 ± 0.11	-1.18 ± 0.04
	$\log \epsilon(Th)_{4086}$	-1.70 ± 0.09	-1.63 ± 0.05	-0.95 ± 0.11	-1.09 ± 0.04
	$\log \epsilon(Th)_{4095}$	-1.76 ± 0.09	-1.57 ± 0.05	-1.01 ± 0.11	-1.10 ± 0.04
	$\log \epsilon(Th)$	-1.79 ± 0.18	-1.63 ± 0.21	-1.06 ± 0.19	-1.12 ± 0.16
Other Work	$\log \epsilon(Eu)$	-1.19 ± 0.10	-0.75 ± 0.10	-0.62 ± 0.05	-0.76 ± 0.13
This Work	$\log \epsilon(Eu)$	-1.16 ± 0.12	-1.16 ± 0.13	-0.53 ± 0.08	-0.81 ± 0.12
<hr/>					
	Chronometer	J0954+5246	J2038-0023	HE 1523-0901	CS 31082-001
Age (Gyr)	U/Th	11.1 ± 6.4	13.5 ± 4.8	16.6 ± 5.1	11.1 ± 4.0
($\pm_{\text{sys}} \pm_{\text{stat}} \pm \text{PR}$)		($\pm 5.7 \pm 1.9 \pm 2.2$)	($\pm 3.8 \pm 2.1 \pm 2.2$)	($\pm 4.2 \pm 2.0 \pm 2.2$)	($\pm 2.8 \pm 1.8 \pm 2.2$)
<hr/>					
Age (Gyr)	U/Eu	12.0 ± 4.3	11.3 ± 3.1	14.2 ± 3.8	7.3 ± 2.6
($\pm_{\text{sys}} \pm_{\text{stat}} \pm \text{PR}$)		($\pm 3.9 \pm 1.0 \pm 1.6$)	($\pm 2.2 \pm 1.4 \pm 1.6$)	($\pm 3.3 \pm 1.0 \pm 1.6$)	($\pm 1.6 \pm 1.3 \pm 1.6$)

NOTE—*Nucleocosmochronometric ages listed are obtained in this work. See text for details on uncertainty estimation for the elemental abundances and stellar ages. Source of other work: ^aHolmbeck et al. (2018), ^bPlacco et al. (2017), ^cFrebel et al. (2007), ^dHill et al. (2002).

fect on the synthetic-spectrum fit to the core of the Th II line. Subsequently, we determined $\log \epsilon(Th)_{4095} = -1.76, -1.57, -1.01$, and -1.10 for J0954+5246, J2038-0023, HE 1523-0901, and CS 31082-001, respectively.

The final Th abundance of each sample star was obtained as the mean of the $\lambda 4019.13$, $\lambda 4086.52$, and $\lambda 4094.75$ Th abundances. We determined mean Th abundance as $\log \epsilon(Th) = -1.79, -1.31, -1.06$, and -1.12 for J0954+5246, J2038-0023, HE 1523-0901, and CS 31082-001, respectively. We list the Th abundances obtained for each line and the corresponding mean Th abundance for each star in Table 5, along with the uncertainty estimates. Table 5 also lists the Th abundances determined in previous literature studies for comparison. For J0954+5246, HE 1523-0901, and CS 31082-001, we obtain good agreement with the Th abundances published in the literature. For J2038-0023, we note some discrepancy, which we attribute to the difference in the adopted stellar parameters (see section 3).

4.4. Europium

We determined the Eu abundance of each sample star using Eu II lines at $\lambda 4219 \text{ \AA}$, $\lambda 4205 \text{ \AA}$, and $\lambda 4435 \text{ \AA}$. We determined the mean $\log \epsilon(Eu) = -1.16, -1.16, -0.53$, and -0.81 for J0954+5246, J2038-0023, HE 1523-0901, and CS 31082-001, respectively. We list the mean Eu abundance, along with the uncertainty estimates and Eu abundance estimates from previous literature studies in Table 5. For J0954+5246, HE 1523-0901, and CS 31082-001, we find our derived Eu abundances to be in good agreement with the literature estimates within uncertainties. For J2038-0023, we note a discrepancy in the abundances, which we attribute to the difference in the adopted stellar parameters.

4.5. Uncertainty Analysis

For the U abundances of the sample stars, we homogeneously accounted for various sources of systematic ($\Delta(\text{sys})$) and statistical ($\Delta(\text{stat})$) uncertainties. For $\Delta(\text{sys})$, we considered the uncertainties on the stellar parameters (T_{eff} , $\log g$, and ξ) and the abundances of the blending elements. We list the individual systematic uncertainty components, ΔT_{eff} , $\Delta \log g$, $\Delta \xi$, and $\Delta(\text{blend})$ in Table 6. For $\Delta(\text{stat})$, we considered the uncertainties on the $\log gf$ values ($\Delta(\log gf)$) and the continuum placement of the synthetic spectra ($\Delta(\text{cont})$), which we also list in Table 6. For each U II line, we estimated the individual uncertainty components, ΔT_{eff} , $\Delta \log g$, $\Delta \xi$, $\Delta(\text{blend})$, $\Delta(\log gf)$, and $\Delta(\text{cont})$.

To estimate U abundance uncertainties from stellar parameters, we independently changed each stellar parameter by its uncertainty. We thus changed T_{eff} by +150 K, $\log g$ by +0.3 dex, and ξ by 0.2 km/s, for all the stars. For every stellar parameter, we re-derived the abundances of key elements and re-synthesized the U II lines. We report the resulting change in the U abundances as ΔT_{eff} , $\Delta \log g$, and $\Delta \xi$, for the respective stellar parameter.

We estimated $\Delta(\text{blend})$ by changing the abundance of the blending element (e.g., Fe and La) by $\pm 1\sigma$ and re-deriving the U abundance. Here σ is the standard deviation in the abundance of the blending element, which we have also adopted as the uncertainty on the mean abundance of the respective blending element (see section 4.1). We further limited the change in the abundance of the blending to ensure that the new synthetic spectrum flux was within the S/N of the observed spectrum. We considered the following blending elements: Fe for the $\lambda 3859 \text{ \AA}$ and $\lambda 4090 \text{ \AA}$ U II lines and La for the $\lambda 4050 \text{ \AA}$ U II line. While the $\lambda 3859 \text{ \AA}$ U II line is also blended with a CN feature, we find that the U abundance determination is most sensitive to the Fe abundance.

We estimated $\Delta(\log gf)$ through varying the $\log gf$ values by the measurement uncertainties listed in Nilsen et al. (2002a) and re-deriving the U abundances. We estimated $\Delta(\text{cont})$ for each U II line by changing the local continuum placement in the spectral synthesis of the U II line by $\pm 0.5\%$ and then re-deriving the U abundance.

We determined the total uncertainty ($\Delta(\text{total})$) on the U abundance of each U II line as quadrature sum of the U II line's systematic and statistical uncertainties. In turn, we determined $\Delta(\text{sys})$ for each U II line as quadrature sum of $\Delta(T_{\text{eff}})$, $\Delta(\log g)$, $\Delta(\xi)$, and $\Delta(\text{blend})$. Similarly, we determined $\Delta(\text{stat})$ for each U II line as quadrature sum of the U II line's $\Delta(\log gf)$

and $\Delta(\text{cont})$. For all the stars, we list the resulting $\Delta(\text{sys})$, $\Delta(\text{stat})$, and $\Delta(\text{total})$ for each U II line in Table 6.

For the final U abundance of each sample star, we take the weighted-average of the U abundances from the three U II lines. Therefore, $\log \epsilon(\text{U}) = \sum_i (w_i \log \epsilon_i) / \sum_i w_i$, where $\log \epsilon_i$ is the U abundance from line i and $w_i = 1/\Delta(\text{stat})_i^2$. Here $\Delta(\text{stat})_i$ is the $\Delta(\text{stat})$ uncertainty as estimated above for the U II line i . We determined the $\Delta(\text{total})$ on the weighted-average U abundance of each star as the quadrature sum of the corresponding $\Delta(\text{sys})$ and $\Delta(\text{stat})$. For the weighted-average U abundance, the systematic uncertainty components, $\Delta(T_{\text{eff}})$, $\Delta(\log g)$, $\Delta(\xi)$, and $\Delta(\text{blend})$ are determined by taking the average of these components estimated for the three U II lines. We then determined $\Delta(\text{sys})$ as the quadrature sum of the averaged $\Delta(T_{\text{eff}})$, $\Delta(\log g)$, $\Delta(\xi)$, and $\Delta(\text{blend})$. For the weighted-average U abundance of each sample star, we determined $\Delta(\text{stat})$ by propagating the $\Delta(\text{stat})$ estimates of each U II for the weighted-average formula i.e., $1/\Delta(\text{stat})^2 = \sum_i w_i$, where $w_i = 1/\Delta(\text{stat})_i^2$. We list the final $\Delta(\text{sys})$, $\Delta(\text{stat})$, and $\Delta(\text{total})$ for the weighted-average U abundance of each star in Table 6.

We also determined systematic and statistical uncertainties for the Th and Eu abundances of all the stars. We determined $\Delta(\text{sys})$ as the quadrature sum of ΔT_{eff} , $\Delta \log g$, and $\Delta \xi$. We determined $\Delta(\text{stat})$ as the standard-error of the mean Th and Eu abundances. Therefore, $\Delta(\text{stat}) = \sigma/n$, where σ is the standard deviation of the abundances determined with different lines and n is the total number of lines used. We then computed $\Delta(\text{total})$ for the mean Th and Eu abundances of all the sample stars as the quadrature sum of the corresponding $\Delta(\text{sys})$ and $\Delta(\text{stat})$.

5. AGES WITH NOVEL U II LINES

The U abundance of a star can be used to determine the star's age using nucleocosmochronometry. We homogeneously determined ages for J0954+5246, J2038-0023, HE 1523-0901, and CS 31082-001, for the first time with U abundance derived using three U II lines. We determined the ages using equations 1 and 2 for the U/Th and U/Eu chronometers, respectively (Cayrel et al. 2001).

$$t = 21.8[\log \epsilon(\text{U/Th})_0 - \log \epsilon(\text{U/Th})_{\text{obs}}] \text{ Gyr} \quad (1)$$

$$t = 14.8[\log \epsilon(\text{U/Eu})_0 - \log \epsilon(\text{U/Eu})_{\text{obs}}] \text{ Gyr} \quad (2)$$

Table 6. Abundance Uncertainties

	ΔT_{eff} (K)	$\Delta \log g$ (cgs)	$\Delta \xi$ (km/s)	$\Delta(\text{blend})$	$\Delta(\text{sys})$	$\Delta \log gf$	$\Delta(\text{cont})$	$\Delta(\text{stat})$	$\Delta(\text{total})$
J0954+5246	+150	+0.30	+0.20	$\pm 1\sigma$			$\pm 0.5\%$		
$\log \epsilon(\text{U})_{3859}$	+0.10	+0.10	+0.05	± 0.23	± 0.27	± 0.05	± 0.10	± 0.11	± 0.30
$\log \epsilon(\text{U})_{4050}$	+0.05	+0.05	+0.02	± 0.30	± 0.31	± 0.03	± 0.10	± 0.10	± 0.33
$\log \epsilon(\text{U})_{4090}$	+0.08	+0.09	+0.04	± 0.23	± 0.26	± 0.06	± 0.15	± 0.15	± 0.30
$\log \epsilon(\text{U})$	+0.08	+0.08	+0.04	± 0.25	± 0.28	± 0.07	± 0.29
$\log \epsilon(\text{Th})$	+0.15	+0.08	+0.00	...	± 0.17	± 0.05	± 0.18
$\log \epsilon(\text{Eu})$	+0.09	+0.07	-0.02	...	± 0.12	± 0.01	± 0.12
$\log \epsilon(\text{U/Th})$	-0.07	+0.00	-0.00	± 0.25	± 0.26	± 0.09	± 0.28
$\log \epsilon(\text{U/Eu})$	-0.01	+0.01	+0.06	± 0.25	± 0.26	± 0.07	± 0.27
J2038-0023	+150	+0.30	+0.20	$\pm 1\sigma$			$\pm 0.5\%$		
$\log \epsilon(\text{U})_{3859}$	+0.10	+0.05	+0.00	± 0.20	± 0.23	± 0.06	± 0.10	± 0.12	± 0.26
$\log \epsilon(\text{U})_{4050}$	+0.04	+0.17	+0.04	± 0.14	± 0.23	± 0.04	± 0.20	± 0.20	± 0.31
$\log \epsilon(\text{U})_{4090}$	+0.10	+0.08	+0.02	± 0.08	± 0.15	± 0.05	± 0.20	± 0.21	± 0.26
$\log \epsilon(\text{U})$	+0.08	+0.10	+0.02	± 0.14	± 0.19	± 0.09	± 0.21
$\log \epsilon(\text{Th})$	+0.18	+0.11	+0.01	...	± 0.21	± 0.03	± 0.21
$\log \epsilon(\text{Eu})$	+0.11	+0.07	+0.00	...	± 0.13	± 0.02	± 0.13
$\log \epsilon(\text{U/Th})$	-0.10	-0.01	+0.01	± 0.14	± 0.17	± 0.10	± 0.20
$\log \epsilon(\text{U/Eu})$	-0.03	+0.03	+0.02	± 0.14	± 0.15	± 0.09	± 0.17
HE 1523-0901	+150	+0.30	+0.20	$\pm 1\sigma$			$\pm 0.5\%$		
$\log \epsilon(\text{U})_{3859}$	+0.10	+0.10	+0.03	± 0.08	± 0.17	± 0.04	± 0.06	± 0.07	± 0.18
$\log \epsilon(\text{U})_{4050}$	+0.01	+0.25	+0.20	± 0.25	± 0.41	± 0.03	± 0.25	± 0.25	± 0.48
$\log \epsilon(\text{U})_{4090}$	+0.10	+0.10	+0.05	± 0.11	± 0.19	± 0.05	± 0.21	± 0.22	± 0.28
$\log \epsilon(\text{U})$	+0.07	+0.15	+0.09	± 0.15	± 0.24	± 0.07	± 0.25
$\log \epsilon(\text{Th})$	+0.14	+0.11	+0.0	...	± 0.18	± 0.06	± 0.19
$\log \epsilon(\text{Eu})$	+0.06	+0.04	-0.03	...	± 0.08	± 0.02	± 0.08
$\log \epsilon(\text{U/Th})$	-0.07	+0.04	+0.09	± 0.15	± 0.19	± 0.09	± 0.21
$\log \epsilon(\text{U/Eu})$	+0.01	+0.11	+0.12	± 0.15	± 0.22	± 0.07	± 0.23
CS 31082-001	+150	+0.30	+0.20	$\pm 1\sigma$			$\pm 0.5\%$		
$\log \epsilon(\text{U})_{3859}$	+0.10	+0.10	+0.00	± 0.13	± 0.19	± 0.05	± 0.10	± 0.11	± 0.22
$\log \epsilon(\text{U})_{4050}$	+0.05	+0.12	+0.03	± 0.10	± 0.17	± 0.03	± 0.13	± 0.13	± 0.21
$\log \epsilon(\text{U})_{4090}$	+0.10	+0.10	+0.00	± 0.07	± 0.16	± 0.06	± 0.18	± 0.19	± 0.25
$\log \epsilon(\text{U})$	+0.08	+0.11	+0.01	± 0.10	± 0.17	± 0.08	± 0.19
$\log \epsilon(\text{Th})$	+0.14	+0.06	-0.02	...	± 0.15	± 0.02	± 0.16
$\log \epsilon(\text{Eu})$	+0.07	+0.08	-0.01	...	± 0.11	± 0.05	± 0.12
$\log \epsilon(\text{U/Th})$	-0.06	+0.05	+0.03	± 0.10	± 0.13	± 0.08	± 0.15
$\log \epsilon(\text{U/Eu})$	+0.01	+0.03	+0.02	± 0.10	± 0.11	± 0.09	± 0.14

Here $\log \epsilon(\text{U/X})_0$ is the production ratio (PR) of the chronometer and $\log \epsilon(\text{U/X})_{\text{obs}}$ is the present-day abundance ratio of the chronometer as determined from this work. We took PRs from [Schatz et al. \(2002\)](#), who used waiting-point calculations to estimate site-independent PRs of r -process elements. We list the final ages from the two chronometers and the associated uncertainties in Table 5. We find the U/Th and U/Eu age agreeing for all the stars within uncertainties. There is a rela-

tively large discrepancy between the U/Th and U/Eu ages of CS 31082-001, which can be attributed to its actinide-boost nature.

We estimated the uncertainty on the ages by propagating the uncertainties of the PRs and the present-day observed abundance ratios. As a result, our age uncertainties consist of statistical, systematic, and PR components. We obtained the uncertainty on the PRs from [Schatz et al. \(2002\)](#), which are 0.10 dex for the U/Th

chronometer and 0.11 dex for the U/Eu chronometer. We determined $\Delta(\text{sys})$ for the present-day abundance ratios as the quadrature sum of the ΔT_{eff} , $\Delta \log g$, $\Delta \xi$, $\Delta(\text{blend})$ uncertainties of the ratios. We determined $\Delta(\text{stat})$ for the present-day abundance-ratios as quadrature sum of $\Delta(\text{stat})$ determined for the elements in the ratio. We list the resulting $\Delta(\text{sys})$ and $\Delta(\text{stat})$ for the present-day U/Th and U/Eu abundance ratios in Table 6. We list the individual systematic, statistical and production-ratio components of the age uncertainties in Table 5. We determined the total uncertainty on the age as the quadrature sum of the systematic, statistical, and production-ratio uncertainties. We further discuss the ages and the respective uncertainties from the various components in Section 6.4.

6. DISCUSSION

To test the reliability of the two new U II lines at $\lambda 4050$ and $\lambda 4090 \text{ \AA}$, we performed the first homogeneous U abundance analysis of four highly RPE stars ($[\text{Eu}/\text{Fe}] > +0.7$) with these new lines, in addition to the canonical $\lambda 3859 \text{ \AA}$ U II line. The stars chosen for the analysis are four of the five stars with U abundance previously determined in the literature. While U abundance was determined for CS 29497-004 (Hill et al. 2017), our analysis of the star’s UVES/VLT spectra indicated an almost-non existent signature of U at all three U II lines. Therefore, we left CS 29497-004 out of further analysis. We now discuss and establish the reliability of the two new U II lines in the other four stars.

6.1. Reliability of the New U II lines: Line Abundances and Uncertainties

Table 5 lists the final U abundance determined at each U II line, along with its estimated uncertainty, for all the sample stars. We note that the U abundances from the three U II lines agree well, within uncertainties, for all the sample stars. We also find that the $\lambda 3859$ U abundance determined in this work is consistent with previous literature estimate of the same within uncertainties for all the stars; $\lambda 3859$ U abundance from literature is also listed in Table 5.

Moreover, we find that in the case for all the sample stars, the uncertainties on the U abundances of all three U II lines are of the same order. This indicates that the new U II lines provide similar precision for U abundance determination as the canonical $\lambda 3859 \text{ \AA}$ U II line. For all three U II lines, we have homogeneously taken into account various sources of systematic and statistical uncertainties (see section 4.5). Generally, we find the systematic uncertainties, specifically, from the blending elements to be the dominant source of the total uncertainty on the U II line abundances. We also find that

U abundance determination with all three U II lines is sensitive to the continuum placement of the synthetic model. The sensitivity of the individual U II lines to the various sources of uncertainties and the similar precision offered by the U II lines impresses upon the advantage of using three U II lines for U abundance determination, instead of just one.

We note, however, an exceptionally high uncertainty estimated for the $\lambda 4050$ U abundance of HE 1523-0901, on the order of ~ 0.5 dex. This high estimate is driven by the La II blend since the star has a relatively strong La feature relative to the other stars (see Figure 2). This does highlight the fact that blends can have a significant impact on U abundance determination. However, we find that the spectral synthesis fit of the region is very good for the derived La abundance of this star.

As noted in section 4.2, even though the spectral synthesis fits to the U II lines are good — the goodness of the fits is further corroborated by the agreement between U abundances from the different U II lines — there is indication of unidentified features in the $\lambda 4090 \text{ \AA}$ and possibly $\lambda 4050 \text{ \AA}$ spectral regions. Given the immense potential of these U II lines on advancing nucleocosmochronometry and r -process studies, we recommend a detailed investigation into the atomic data, especially laboratory measurements of the transition lines in these spectral regions.

6.2. Reliability of the New U II lines: Residuals between Line Abundances

We further demonstrate the reliability of the new U II lines with Figure 6, which shows (i) the residuals between the $\lambda 4050$ and $\lambda 3859$ U abundances in circle data points and (ii) the residuals between the $\lambda 4090$ and $\lambda 3859$ U abundances in square data points, for all the sample stars. The residuals are plotted against the respective star’s T_{eff} , $\log g$, $[\text{Fe}/\text{H}]$, $[\text{C}/\text{Fe}]$, $[\text{Eu}/\text{Fe}]$, and spectrum S/N in different panels. The uncertainties on the residual data points are calculated by propagating the total uncertainties of the individual line abundances.

First, we note that the residuals of the U abundances are all within ± 0.2 dex (shown by the shaded grey region) for all the stars. For CS 31082-001, while we find that the residual between the $\lambda 4090$ and $\lambda 3859$ U abundances is 0.0 dex, the residual between the $\lambda 4050$ and $\lambda 3859$ U abundances is +0.40 dex. This indicates that there might be an unidentified transition line in the $\lambda 4050 \text{ \AA}$ U II line region that is more prominent for CS 31082-001 than for the other stars. Alternatively, the abundance of the La II HFS structure in this region may not be well represented by the mean La abundance determined for the star. While this relatively large residual

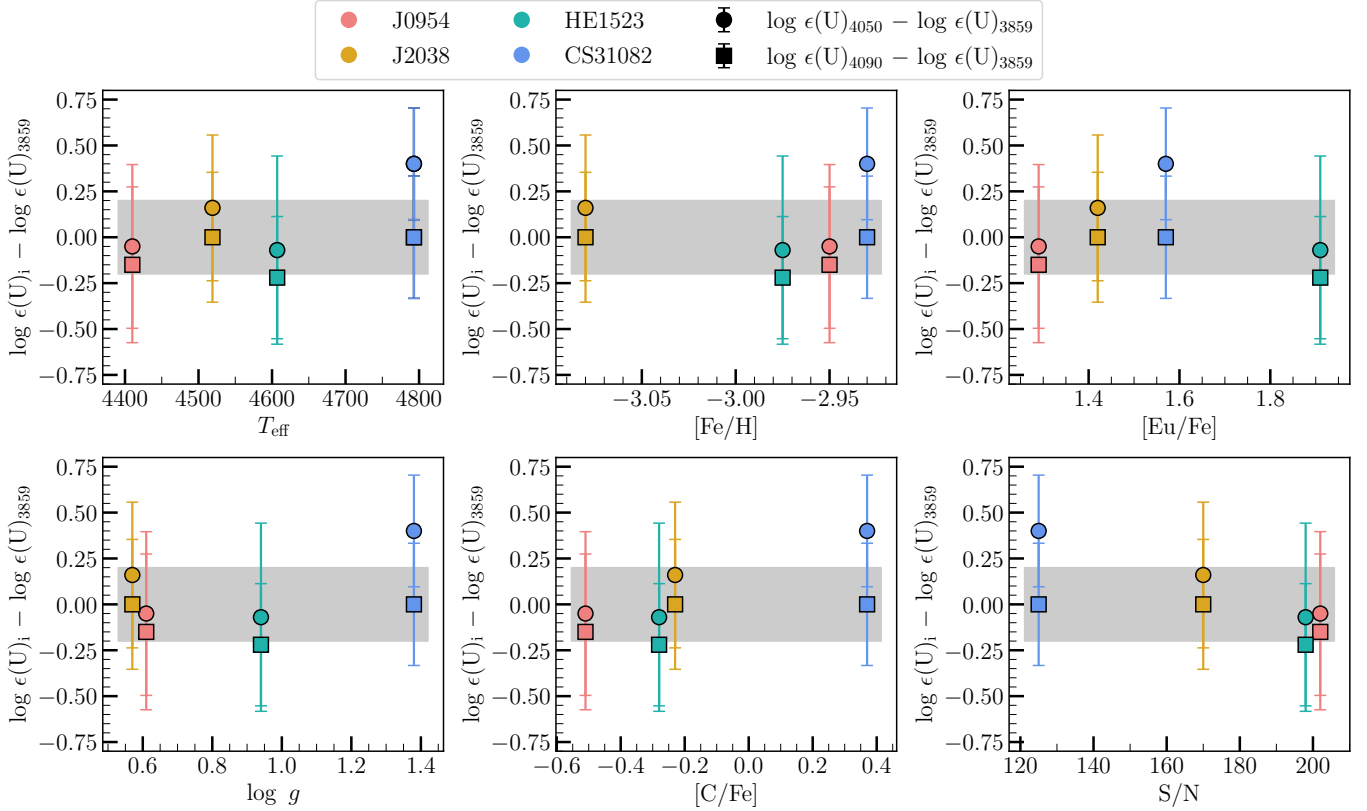


Figure 6. For all the sample stars, residuals between the $\lambda 4050 \text{ \AA}$ and $\lambda 3859 \text{ \AA}$ U II line abundances are shown with round data points and the residuals between the $\lambda 4090 \text{ \AA}$ and $\lambda 3859 \text{ \AA}$ U II line abundances are shown with square data points. The residuals are plotted against the T_{eff} , $\log g$, $[\text{Fe}/\text{H}]$, $[\text{C}/\text{Fe}]$, and S/N at 4050 \AA of the respective stars in different panels. A grey-shaded region for residuals within ± 0.2 dex is also shown.

may signify the need to better constrain the atomic data of this spectral region and/or the abundance of the La II HFS structure, the uncertainty on the residual overlaps with the ± 0.2 dex shaded-region, subduing any serious concern.

Second, we note that the residuals of the U abundances show no discernible trend with respect to T_{eff} , $\log g$, $[\text{Fe}/\text{H}]$, $[\text{C}/\text{Fe}]$, $[\text{Eu}/\text{Fe}]$, and spectrum S/N. This indicates that our current spectral synthesis models are of high fidelity and no identifiable systematic biases are being percolated to the U abundance determinations. Together, the ± 0.2 dex range of the residuals between the U II line abundances and the absence of any significant trend in the residuals with respect to key atmospheric and chemical properties as well as data-quality of the sample stars establishes the reliability of the two new U II new lines at $\lambda 4050 \text{ \AA}$ and $\lambda 4090 \text{ \AA}$.

6.3. Mean U Abundance with Multiple U II lines

We provide revised U abundances for the RPE stars, J0954+5246, J2038-0023, HE 1523-0901, and CS 31082-001 via a homogeneous analysis of the three U II lines at $\lambda 3859 \text{ \AA}$, $\lambda 4050 \text{ \AA}$, and $\lambda 4090 \text{ \AA}$. The resulting mean U

abundance is computed as a weighted-average of the U abundances from the three U II lines, with the weights assigned based on the statistical uncertainty on the U abundance of each line (see section 4.2 for more details). We find that the total uncertainty of the weighted-average U abundances is on the order of ~ 0.2 dex, for all sample stars. On the other hand, the total uncertainty of individual U II line abundances is higher and typically in the range of $\sim 0.2 - 0.3$ dex. This reiterates the advantage of using multiple U II lines, which can potentially lend more precise U abundance than a single U II line.

We compare the final weighted-average U abundances estimated in this work to previous literature estimates of $\lambda 3859$ U abundances in Figure 7, for all the stars. We find that our U abundances agree well with the literature values within uncertainties, for all the stars. In fact, the final U abundances agree with previous literature estimates within 0.05 dex for HE 1523-0901 and CS 31082-001, which we consider excellent agreement. This further establishes the reliability of the new U II lines. For J0954+5246, we find that our U abundance is ~ 0.4 dex lower than that determined by Holmbeck et al.

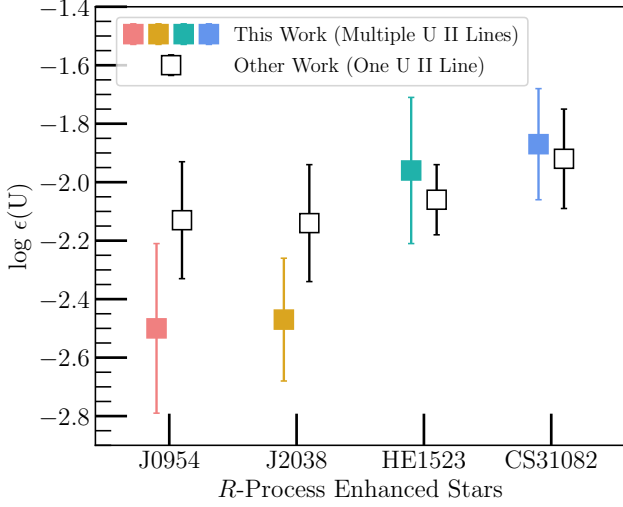


Figure 7. Weighted-average U abundances derived in this work with U II lines at $\lambda 3859$, $\lambda 4050$, and $\lambda 4090$ Å for J0954+5246, J2038-0023, HE 1523-0901, and CS 31082-001. U abundances determined in previous literature studies using the $\lambda 3859$ Å line are also shown. Literature U abundance was taken from Holmbeck et al. (2018) for J0954+5246, Placco et al. (2017) for J2038-0023, Frebel et al. (2007) for HE 1523-0901, and Hill et al. (2002) for CS 31082-001.

(2018). We investigated the source of this discrepancy and suspect the cause to be differences in the adopted atomic data of the $\lambda 3859.91$ Å Fe I line. We also find that our U abundance for J2038-0023 is ~ 0.3 dex lower than that determined by Placco et al. (2017). This discrepancy is attributed to the difference in the adopted stellar parameters, especially $\log g$ (see section 3). Nevertheless, our U/Th and U/Eu nucleocosmochronometric age estimates compare well with those reported in Placco et al. (2017) (see section 5).

We also discuss the uncertainty estimates on the final U abundances as determined in this work compared to previous literature estimates. In the case of J0954+5246 and HE 1523-0901, the total uncertainty estimated for the final weighted-average U abundance in this work is larger than the uncertainty quoted by the respective previous literature studies for their final $\lambda 3859$ U abundance (see Figure 7 and/or Table 5). For J0954+5246, Holmbeck et al. (2018) quoted a fiducial uncertainty of ± 0.20 dex on their final U abundance, while we obtained an uncertainty of ± 0.29 dex. For HE 1523-0901, Frebel et al. (2007) assigned an uncertainty of ± 0.11 dex, solely arising from the effect of changing the Fe abundance by ± 0.10 dex (although they considered additional sources of uncertainties in the age determinations). Having accounted for additional sources of uncertainties, we obtained a larger uncertainty of ± 0.25 dex for the U abundance of HE 1523-0901. While Placco et al. (2017) also

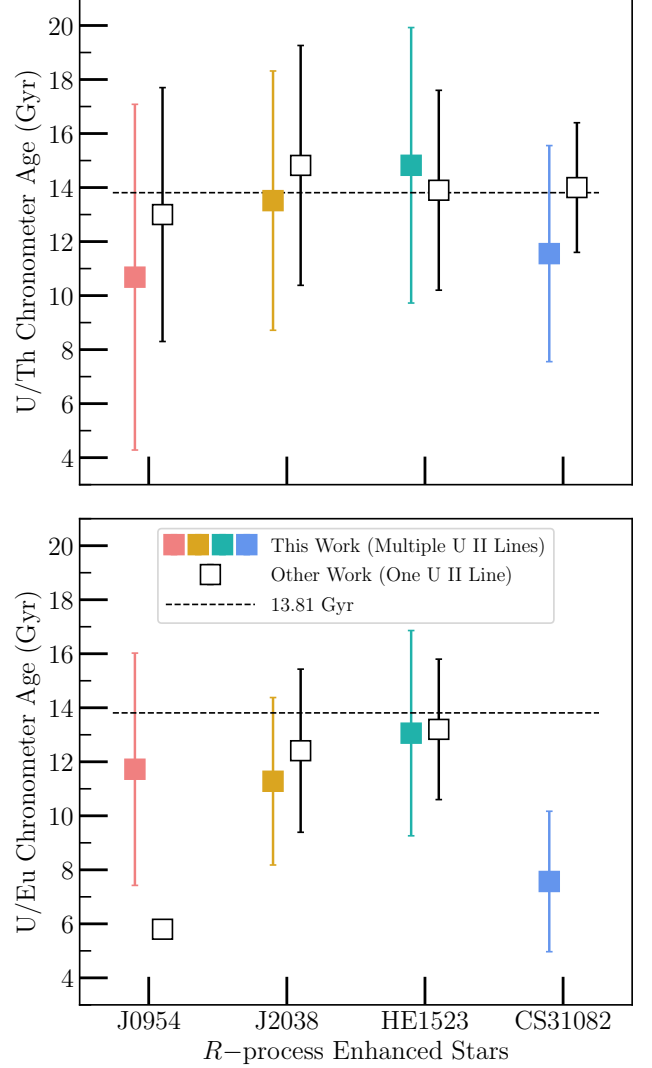


Figure 8. Nucleocosmochronometric ages from this work (colored data points) and previous literature work (white data points) using the U/Th (top panel) and U/Eu (bottom panel) chronometers. The age of the universe is shown in dashed-black line (Planck Collaboration et al. 2016). For the ages of this work, the weighted-average U, Th, and Eu abundances from multiple transition lines were used. Literature ages were taken from Holmbeck et al. (2018) for J0954+5246, Placco et al. (2017) for RAVE J203843.2-002333, Frebel et al. (2007) for HE 1523-0901, and Hill et al. (2002) for CS 31082-001.

set a fiducial uncertainty of ± 0.20 dex for J2038-0023, we find our detailed analysis renders a similar uncertainty of ± 0.21 dex. Similarly for CS 31082-001, we find that our U abundance uncertainty of ± 0.19 dex agrees with that of Hill et al. (2002), who also accounted for stellar parameters, oscillator strength, and observational fitting uncertainties and obtained an uncertainty of ± 0.19 dex.

6.4. Ages with Mean U Abundances

For every sample star, we determined two stellar ages, one from the U/Th chronometer and another using the U/Eu chronometer. We list the resulting ages in Table 5. There is a good agreement between the U/Th and U/Eu ages of J0954+5246, J2038-0023, and HE 1523-0901. For CS 31082-001, U/Eu age is ~ 4.0 Gyr lower than the U/Th age due to its actinide-boost nature (Cayrel et al. 2001; Hill et al. 2002; Schatz et al. 2002). Even then, the U/Th and U/Eu ages of CS 31082-001 agree within uncertainties.

For stellar age uncertainties, we took into account systematic, statistical, and PR uncertainties as described in section 5. These individual age uncertainty components are also listed in Table 5, along with the total age uncertainties. For the U/Th and U/Eu stellar ages of all the sample stars, the systematic uncertainties are the largest (and also the most dominant, in many cases), followed by the PR uncertainties and then the statistical uncertainties. Specifically, the systematic uncertainties of the stellar ages are driven by the large U abundance uncertainties from the blending elements.

Additionally, the uncertainties on the U/Th stellar ages are larger than the U/Eu counterpart because of the longer half-life of Th, relative to U. We note that we have not taken into account the systematic uncertainties associated with using just one set of theoretical PRs (from Schatz et al. 2002). Other r -process models have predicted slightly varying zero-age abundance ratios for U/Th and U/Eu (e.g., Goriely & Arnould 2001; Farouqi et al. 2010). However, since the aim of this study was to investigate stellar ages estimated with revised U abundances from multiple U II lines, we find using one set of PRs sufficient for the analysis.

We compare all the stellar ages determined in this work to previous literature results in Figure 8, which shows the U/Th and U/Eu ages in the top and bottom panels, respectively. The dashed black line in Figure 8 indicates the age of the universe, as determined by the *Planck* mission (Planck Collaboration et al. 2016). For the literature ages of J0954+5246 (Holmbeck et al. 2018), J2038-0023 (Placco et al. 2017), and HE 1523-0901 (Frebel et al. 2007), we display the ages determined by the respective studies using, specifically, the zero-age abundance ratios of Schatz et al. (2002) to facilitate a consistent comparison to our age-estimates. For CS 31082-001, Hill et al. (2002) determined U/Th age using zero-age abundance ratio from Goriely & Arnould (2001), which we display. Also, Hill et al. (2002) did not determine the U/Eu stellar age of the CS 31082-001.

We find that our stellar ages mostly agree well with previous literature results within uncertainties. The ex-

ception to this case is the U/Eu age of J0954+5246, which is much higher than previously determined in the literature. We attribute this discrepancy to a lower U abundance determined in this work relative to that determined in Holmbeck et al. (2018) (see section 6.3 more details). We also determined lower Th abundance relative to Holmbeck et al. (2018) so that in the U/Th ratio, the offset in the abundances is cancelled.

7. CONCLUSIONS

Uranium abundances of metal-poor RPE stars enable stellar age determination independent from stellar evolution models, using nucleocosmochronometry. U abundances of a large sample of RPE stars may also enable important constraints on the astrophysical conditions and nuclear physics of r -process enrichment events, by probing the production of the actinides. However, U abundance determination has been limited to using a single U II line at $\lambda 3859$ Å. In this study, we have performed the first homogeneous U abundance analysis of four highly RPE stars with two new U II lines at $\lambda 4050$ Å and $\lambda 4090$ Å, along with the canonical $\lambda 3859$ Å U II line.

We test the utility of the $\lambda 4050$ Å and $\lambda 4090$ Å U II lines and find them generally reliable for U abundance determination. In Figures 2 and 3, we show the spectral synthesis fits to the new U II lines. The resulting $\lambda 3859$, $\lambda 4050$, and $\lambda 4090$ U abundances agree with each other within ± 0.2 dex for most stars, and within uncertainties for all the stars, as seen in Figure 6. In fact, we find it particularly advantageous to use the $\lambda 4050$ Å and $\lambda 4090$ Å U II lines, since they are not blended with strong lines or C features. In that regard, they may find a special utility for determining U abundances of C-enhanced metal-poor stars. As seen in Figure 7, the final weighted-average U abundances of all the sample stars agree with previous literature estimates. This substantiates our U abundance analysis framework and the use of multiple U II lines.

We performed a detailed uncertainty analysis of the U abundances by taking into account systematic uncertainties from stellar parameters and blends, as well as statistical uncertainties from continuum placement and $\log gf$ measurements. We find that all three U II lines provide similar precision of ~ 0.2 – 0.3 dex. On the other hand, for the weighted-average U abundance, the uncertainties are on the order of ~ 0.2 dex. This underscores the advantage of using multiple U II lines. Moreover, any unconstrained systematic biases associated with a particular U II line are mitigated in the average abundance from multiple U II lines.

We also obtained homogeneous ages for the stars with the U/Th and U/Eu chronometers and using the U, Th,

and Eu abundances as derived in this work from multiple transition lines of each element. As seen in Figure 8, we find that the newly obtained ages are reasonable and in agreement with previous literature estimates within uncertainties. For the uncertainties on the ages, we estimated the systematic, statistical, and PR uncertainty components for all the stars. The resulting total uncertainties on the ages of the sample stars are on the order of $\sim 4 - 6$ Gyr for the U/Th ages and $\sim 3 - 4$ Gyr for the U/Eu ages.

To improve the uncertainties on the U abundances and subsequently stellar ages, it will be necessary to address systematic uncertainties from the blends and stellar parameters. Additionally, a substantial component of U abundance uncertainties is contributed to fitting uncertainties like continuum placement. As a result, studies of these new U II-line spectral regions are recommended to better constrain the atomic parameters of the blends and to identify unknown neighboring transitions, which will improve the confidence in the continuum placement.

Another source of uncertainty on the stellar ages is the poorly known nuclear physics that enters into the predicted U/Th and U/Eu PRs. Upcoming studies at facilities such as the N=126 Factory at Argonne National Laboratory (Savard et al. 2020) and the Facility for Rare Isotope Beams (Castelvecchi 2022) will reach many heavy, neutron-rich species whose properties are crucial for understanding actinide production. These anticipated advances in atomic and nuclear physics will contribute to the overarching goal of improving the precision of nucleocosmochronometry.

Through the rest of the decade, we are expecting an influx of new spectroscopic data, specifically for RPE stars, from surveys such as that by the *R*-Process Alliance (Hansen et al. 2018; Sakari et al. 2018; Ezzeddine et al. 2020; Holmbeck et al. 2020), 4MOST (de Jong et al. 2019), and WEAVE (Dalton et al. 2012). Reliable U abundance determination of RPE stars will be critical in obtaining precise and robust nucleocosmochronometric ages of some of the oldest stars. Precise nucleocosmochronometric ages, combined with chemo-dynamical information, can aid our understanding of the chemical enrichment and evolution in the early Universe, especially of the *r*-process elements, as well as the assembly history of our galaxy. Additionally, reliable U abundances for a large sample of RPE stars can shed light on the extent of actinide-variation in RPE stars and its origin. To that end, the results of this work open up a new avenue to reliably determine U abundances and nucleocosmochronometric ages for a large sample of RPE stars with multiple U II lines.

SPS acknowledges Jamie Tayar for useful conversations on stellar ages and other comments. RE acknowledges support from NSF grant AST-2206263. APJ was supported by NASA through Hubble Fellowship grant HST-HF2-51393.001 awarded by the Space Telescope Science Institute, which is operated by the Association of Universities for Research in Astronomy, Inc., for NASA, under contract NAS5-26555. APJ also acknowledges support from a Carnegie Fellowship and the Thatcher Research Award in Astronomy. T.T.H acknowledges support from the Swedish Research Council (VR 2021-05556). This project initiated during MC’s 2018 sabbatical stay at Carnegie Observatories, and he is very grateful to the faculty and staff there for their hospitality and generous support. Additional support for MC is provided by the Ministry for the Economy, Development, and Tourism’s Millennium Science Initiative through grant ICN12_12009, awarded to the Millennium Institute of Astrophysics (MAS), and by Proyecto Basal CATA ACE210002 and FB210003. I.U.R. acknowledges support from the U.S. National Science Foundation (NSF) (grants PHY 14-30152—Physics Frontier Center/JINA-CEE, AST 1815403/1815767, and AST 2205847), and the NASA Astrophysics Data Analysis Program, grant 80NSSC21K0627. EMH acknowledges support for this work provided by NASA through the NASA Hubble Fellowship grant HST-HF2-51481.001 awarded by the Space Telescope Science Institute, which is operated by the Association of Universities for Research in Astronomy, Inc., for NASA, under contract NAS5-26555. T.C.B. acknowledges partial support for this work from grant PHY 14-30152; Physics Frontier Center/JINA Center for the Evolution of the Elements (JINA-CEE), awarded by the US National Science Foundation. This work has made use of data from the European Space Agency (ESA) mission *Gaia* (<https://www.cosmos.esa.int/gaia>), processed by the *Gaia* Data Processing and Analysis Consortium (DPAC, <https://www.cosmos.esa.int/web/gaia/dpac/consortium>). Funding for the DPAC has been provided by national institutions, in particular the institutions participating in the *Gaia* Multilateral Agreement. The authors wish to recognize and acknowledge the very significant cultural role and reverence that the summit of Maunakea has always had within the indigenous Hawaiian community. We are most fortunate to have the opportunity to conduct observations from this mountain.

Facilities: Keck/HIRES, Magellan/MIKE,
VLT/UVES

Table A1. Hyperfine Structure Line Component Pattern for the La II $\lambda 4050$ Line

Wavenumber (cm^{-1})	λ_{air} (\AA)	F_{upper}	F_{lower}	Component Position (cm^{-1})	Component Position (\AA)	Strength
24683.94	4050.073	5.5	6.5	+0.188754	-0.030979	0.25000
24683.94	4050.073	5.5	5.5	+0.097552	-0.016010	0.04545
24683.94	4050.073	5.5	4.5	+0.018860	-0.003095	0.00455
24683.94	4050.073	4.5	5.5	+0.066181	-0.010862	0.16883
24683.94	4050.073	4.5	4.5	-0.012510	+0.002053	0.06926
24683.94	4050.073	4.5	3.5	-0.077930	+0.012790	0.01190
24683.94	4050.073	3.5	4.5	-0.037194	+0.006104	0.10476
24683.94	4050.073	3.5	3.5	-0.102614	+0.016842	0.07483
24683.94	4050.073	3.5	2.5	-0.154142	+0.025298	0.02041
24683.94	4050.073	2.5	3.5	-0.121201	+0.019892	0.05612
24683.94	4050.073	2.5	2.5	-0.172729	+0.028349	0.06531
24683.94	4050.073	2.5	1.5	-0.209879	+0.034446	0.02857
24683.94	4050.073	1.5	2.5	-0.185678	+0.030474	0.02143
24683.94	4050.073	1.5	1.5	-0.222828	+0.036572	0.04286
24683.94	4050.073	1.5	0.5	-0.245257	+0.040253	0.03571

NOTE—Energy levels from the NIST ASD and the index of air (Peck & Reeder 1972) are used to compute the center-of-gravity wavenumbers and air wavelengths, λ_{air} . Line component positions are given relative to those values. Component strengths are normalized to sum to 1.0.

Software: `astropy` (Astropy Collaboration et al. 2013), `MAKEE` (<https://sites.astro.caltech.edu/~tb/makee/>), `CarPy` (Kelson et al. 2000; Kelson 2003), `ESOReflex` (Freudling et al. 2013), `MOOG` (<https://github.com/alexji/moog17scat> and Snen (1973)), `SMHr` (<https://github.com/eholmbeck/smhr-rpa/tree/refactor-scatterplot> and <https://github.com/andycasey/smhr/tree/refactor-scatterplot>)

APPENDIX

A. HYPERFINE SPLITTING OF THE LA II $\lambda 4050$ LINE

The U II line at 4050.04 \AA is blended with a stronger La II line at 4050.073 \AA . There is one dominant naturally occurring isotope of La, ^{139}La , which has nuclear spin $I = 7/2$. This non-zero nuclear spin creates HFS structure, which desaturates the line and is thus important to account for in stellar abundance work. We adopt the HFS A and B constants for the upper and lower levels of this transition from the measurements of Furmann et al. (2008b,a). We compute the complete line component pattern for this line following the procedure described in Appendix A1 of Ivans et al. (2006). We calculate the center-of-gravity wavenumber of this line from the energy levels given in the National Institute of Standards and Technology (NIST) Atomic Spectra Database (ASD; Kramida et al. 2021). We convert to the center-of-gravity air wavelength using the standard index of air (Peck & Reeder 1972). Table A1 lists the line component positions relative to these values. The strengths are normalized to sum to 1.0.

REFERENCES

- Abdalla, E., Abellán, G. F., Aboubrahim, A., et al. 2022, *Journal of High Energy Astrophysics*, 34, 49, doi: [10.1016/j.jheap.2022.04.002](https://doi.org/10.1016/j.jheap.2022.04.002)
- Arnould, M., & Goriely, S. 2020, *Progress in Particle and Nuclear Physics*, 112, 103766, doi: [10.1016/j.ppnp.2020.103766](https://doi.org/10.1016/j.ppnp.2020.103766)

- Arnould, M., & Takahashi, K. 1999, Reports on Progress in Physics, 62, 395, doi: [10.1088/0034-4885/62/3/003](https://doi.org/10.1088/0034-4885/62/3/003)
- Astropy Collaboration, Robitaille, T. P., Tollerud, E. J., et al. 2013, A&A, 558, A33, doi: [10.1051/0004-6361/201322068](https://doi.org/10.1051/0004-6361/201322068)
- Beers, T. C., & Christlieb, N. 2005, Annual Review of Astronomy and Astrophysics, 43, 531, doi: [10.1146/annurev.astro.42.053102.134057](https://doi.org/10.1146/annurev.astro.42.053102.134057)
- Bernstein, R., Sheckman, S. A., Gunnels, S. M., Mochnacki, S., & Athey, A. E. 2003, in Society of Photo-Optical Instrumentation Engineers (SPIE) Conference Series, Vol. 4841, Instrument Design and Performance for Optical/Infrared Ground-based Telescopes, ed. M. Iye & A. F. M. Moorwood, 1694–1704, doi: [10.1117/12.461502](https://doi.org/10.1117/12.461502)
- Bonaca, A., Conroy, C., Cargile, P. A., et al. 2020, ApJL, 897, L18, doi: [10.3847/2041-8213/ab9caa](https://doi.org/10.3847/2041-8213/ab9caa)
- Bond, H. E., Nelan, E. P., VandenBerg, D. A., Schaefer, G. H., & Harmer, D. 2013, ApJL, 765, L12, doi: [10.1088/2041-8205/765/1/L12](https://doi.org/10.1088/2041-8205/765/1/L12)
- Bord, D. J., Barisciano, L. P., J., & Cowley, C. R. 1996, MNRAS, 278, 997, doi: [10.1093/mnras/278.4.997](https://doi.org/10.1093/mnras/278.4.997)
- Buder, S., Lind, K., Ness, M. K., et al. 2022, MNRAS, 510, 2407, doi: [10.1093/mnras/stab3504](https://doi.org/10.1093/mnras/stab3504)
- Burbidge, E. M., Burbidge, G. R., Fowler, W. A., & Hoyle, F. 1957, Reviews of Modern Physics, 29, 547, doi: [10.1103/RevModPhys.29.547](https://doi.org/10.1103/RevModPhys.29.547)
- Cameron, A. G. W. 1957, PASP, 69, 201, doi: [10.1086/127051](https://doi.org/10.1086/127051)
- Casey, A. R. 2014, PhD thesis, Australian National University, Canberra
- Castelli, F., & Kurucz, R. L. 2003, in Modelling of Stellar Atmospheres, ed. N. Piskunov, W. W. Weiss, & D. F. Gray, Vol. 210, A20. <https://arxiv.org/abs/astro-ph/0405087>
- Castelvecchi, D. 2022, Nature, 605, 201, doi: [10.1038/d41586-022-00711-5](https://doi.org/10.1038/d41586-022-00711-5)
- Catelan, M. 2018, in Rediscovering Our Galaxy, ed. C. Chiappini, I. Minchev, E. Starkenburg, & M. Valentini, Vol. 334, 11–20, doi: [10.1017/S1743921318000868](https://doi.org/10.1017/S1743921318000868)
- Cayrel, R., Hill, V., Beers, T. C., et al. 2001, Nature, 409, 691. <https://arxiv.org/abs/astro-ph/0104357>
- Corliss, C. H., & Bozman, W. R. 1962, NBS Monograph, Vol. 53, Experimental transition probabilities for spectral lines of seventy elements; derived from the NBS Tables of spectral-line intensities, ed. Corliss, C. H. & Bozman, W. R. (US Government Printing Office)
- Cowan, J. J., McWilliam, A., Sneden, C., & Burris, D. L. 1997, ApJ, 480, 246, doi: [10.1086/303968](https://doi.org/10.1086/303968)
- Cowan, J. J., Pfeiffer, B., Kratz, K. L., et al. 1999, ApJ, 521, 194, doi: [10.1086/307512](https://doi.org/10.1086/307512)
- Cowan, J. J., Thielemann, F.-K., & Truran, J. W. 1991, ARA&A, 29, 447, doi: [10.1146/annurev.aa.29.090191.002311](https://doi.org/10.1146/annurev.aa.29.090191.002311)
- Dalton, G., Trager, S. C., Abrams, D. C., et al. 2012, in Society of Photo-Optical Instrumentation Engineers (SPIE) Conference Series, Vol. 8446, Ground-based and Airborne Instrumentation for Astronomy IV, ed. I. S. McLean, S. K. Ramsay, & H. Takami, 84460P, doi: [10.1117/12.925950](https://doi.org/10.1117/12.925950)
- de Jong, R. S., Agertz, O., Berbel, A. A., et al. 2019, The Messenger, 175, 3, doi: [10.18727/0722-6691/5117](https://doi.org/10.18727/0722-6691/5117)
- Dekker, H., D’Odorico, S., Kaufer, A., Delabre, B., & Kotzlowski, H. 2000, in Society of Photo-Optical Instrumentation Engineers (SPIE) Conference Series, Vol. 4008, Optical and IR Telescope Instrumentation and Detectors, ed. M. Iye & A. F. Moorwood, 534–545, doi: [10.1117/12.395512](https://doi.org/10.1117/12.395512)
- Epstein, C. R., Elsworth, Y. P., Johnson, J. A., et al. 2014, ApJL, 785, L28, doi: [10.1088/2041-8205/785/2/L28](https://doi.org/10.1088/2041-8205/785/2/L28)
- Ezzeddine, R., Rasmussen, K., Frebel, A., et al. 2020, ApJ, 898, 150, doi: [10.3847/1538-4357/ab9d1a](https://doi.org/10.3847/1538-4357/ab9d1a)
- Farouqi, K., Kratz, K. L., Pfeiffer, B., et al. 2010, ApJ, 712, 1359, doi: [10.1088/0004-637X/712/2/1359](https://doi.org/10.1088/0004-637X/712/2/1359)
- Francois, P., Spite, M., & Spite, F. 1993, A&A, 274, 821
- Frebel, A. 2018, Annual Review of Nuclear and Particle Science, 68, 237, doi: [10.1146/annurev-nucl-101917-021141](https://doi.org/10.1146/annurev-nucl-101917-021141)
- Frebel, A., Casey, A. R., Jacobson, H. R., & Yu, Q. 2013, ApJ, 769, 57, doi: [10.1088/0004-637X/769/1/57](https://doi.org/10.1088/0004-637X/769/1/57)
- Frebel, A., Christlieb, N., Norris, J. E., et al. 2007, ApJL, 660, L117, doi: [10.1086/518122](https://doi.org/10.1086/518122)
- Frebel, A., & Kratz, K.-L. 2009, in The Ages of Stars, ed. E. E. Mamajek, D. R. Soderblom, & R. F. G. Wyse, Vol. 258, 449–456, doi: [10.1017/S1743921309032104](https://doi.org/10.1017/S1743921309032104)
- Freudling, W., Romaniello, M., Bramich, D. M., et al. 2013, A&A, 559, A96, doi: [10.1051/0004-6361/201322494](https://doi.org/10.1051/0004-6361/201322494)
- Furmann, B., Elantkowska, M., Stefańska, D., Ruczkowski, J., & Dembczyński, J. 2008a, Journal of Physics B Atomic Molecular Physics, 41, 235002, doi: [10.1088/0953-4075/41/23/235002](https://doi.org/10.1088/0953-4075/41/23/235002)
- Furmann, B., Ruczkowski, J., Stefańska, D., Elantkowska, M., & Dembczyński, J. 2008b, Journal of Physics B Atomic Molecular Physics, 41, 215004, doi: [10.1088/0953-4075/41/21/215004](https://doi.org/10.1088/0953-4075/41/21/215004)
- Goriely, S., & Arnould, M. 2001, A&A, 379, 1113, doi: [10.1051/0004-6361:20011368](https://doi.org/10.1051/0004-6361:20011368)
- Goriely, S., & Clerbaux, B. 1999, A&A, 346, 798. <https://arxiv.org/abs/astro-ph/9904409>

- Hansen, T. T., Holmbeck, E. M., Beers, T. C., et al. 2018, *ApJ*, 858, 92, doi: [10.3847/1538-4357/aabacc](https://doi.org/10.3847/1538-4357/aabacc)
- Hill, V., Christlieb, N., Beers, T. C., et al. 2017, *A&A*, 607, A91, doi: [10.1051/0004-6361/201629092](https://doi.org/10.1051/0004-6361/201629092)
- Hill, V., Plez, B., Cayrel, R., et al. 2002, *A&A*, 387, 560, doi: [10.1051/0004-6361:20020434](https://doi.org/10.1051/0004-6361:20020434)
- Holmbeck, E. M., Frebel, A., McLaughlin, G. C., et al. 2019a, *ApJ*, 881, 5, doi: [10.3847/1538-4357/ab2a01](https://doi.org/10.3847/1538-4357/ab2a01)
- Holmbeck, E. M., Sprouse, T. M., Mumpower, M. R., et al. 2019b, *ApJ*, 870, 23, doi: [10.3847/1538-4357/aaefef](https://doi.org/10.3847/1538-4357/aaefef)
- Holmbeck, E. M., Beers, T. C., Roederer, I. U., et al. 2018, *ApJL*, 859, L24, doi: [10.3847/2041-8213/aac722](https://doi.org/10.3847/2041-8213/aac722)
- Holmbeck, E. M., Hansen, T. T., Beers, T. C., et al. 2020, *ApJS*, 249, 30, doi: [10.3847/1538-4365/ab9c19](https://doi.org/10.3847/1538-4365/ab9c19)
- Ivans, I. I., Simmerer, J., Sneden, C., et al. 2006, *ApJ*, 645, 613, doi: [10.1086/504069](https://doi.org/10.1086/504069)
- Ji, A. P., & Frebel, A. 2018, *ApJ*, 856, 138, doi: [10.3847/1538-4357/aab14a](https://doi.org/10.3847/1538-4357/aab14a)
- Ji, A. P., Simon, J. D., Frebel, A., Venn, K. A., & Hansen, T. T. 2019, *ApJ*, 870, 83, doi: [10.3847/1538-4357/aaf3bb](https://doi.org/10.3847/1538-4357/aaf3bb)
- Jimenez, R., Cimatti, A., Verde, L., Moresco, M., & Wandelt, B. 2019, *JCAP*, 2019, 043, doi: [10.1088/1475-7516/2019/03/043](https://doi.org/10.1088/1475-7516/2019/03/043)
- Joyce, M., & Chaboyer, B. 2015, *ApJ*, 814, 142, doi: [10.1088/0004-637X/814/2/142](https://doi.org/10.1088/0004-637X/814/2/142)
- Kelson, D. D. 2003, *PASP*, 115, 688, doi: [10.1086/375502](https://doi.org/10.1086/375502)
- Kelson, D. D., Illingworth, G. D., van Dokkum, P. G., & Franx, M. 2000, *ApJ*, 531, 159, doi: [10.1086/308445](https://doi.org/10.1086/308445)
- Kramida, A., Ralchenko, Y., Reader, J., & NIST ASD Team. 2021, NIST Atomic Spectra Database (ver. 5.9), [Online]. Available: <https://physics.nist.gov/asd>, National Institute of Standards and Technology, Gaithersburg, MD.
- Lund, K. A., Engel, J., McLaughlin, G. C., et al. 2022, *arXiv e-prints*, arXiv:2208.06373, <https://arxiv.org/abs/2208.06373>
- Lundberg, H., Johansson, S., Nilsson, H., & Zhang, Z. 2001, *A&A*, 372, L50, doi: [10.1051/0004-6361:20010608](https://doi.org/10.1051/0004-6361:20010608)
- Marín-Franch, A., Aparicio, A., Piotto, G., et al. 2009, *ApJ*, 694, 1498, doi: [10.1088/0004-637X/694/2/1498](https://doi.org/10.1088/0004-637X/694/2/1498)
- Mashonkina, L., Christlieb, N., & Eriksson, K. 2014, *A&A*, 569, A43, doi: [10.1051/0004-6361/201424017](https://doi.org/10.1051/0004-6361/201424017)
- Masseron, T., Plez, B., Van Eck, S., et al. 2014, *A&A*, 571, A47, doi: [10.1051/0004-6361/201423956](https://doi.org/10.1051/0004-6361/201423956)
- McWilliam, A., Preston, G. W., Sneden, C., & Searle, L. 1995, *AJ*, 109, 2757, doi: [10.1086/117486](https://doi.org/10.1086/117486)
- Miglio, A., Chiappini, C., Morel, T., et al. 2013, in *European Physical Journal Web of Conferences*, Vol. 43, European Physical Journal Web of Conferences, 03004, doi: [10.1051/epjconf/20134303004](https://doi.org/10.1051/epjconf/20134303004)
- Nilsson, H., Ivarsson, S., Johansson, S., & Lundberg, H. 2002a, *A&A*, 381, 1090, doi: [10.1051/0004-6361:20011540](https://doi.org/10.1051/0004-6361:20011540)
- Nilsson, H., Zhang, Z. G., Lundberg, H., Johansson, S., & Nordström, B. 2002b, *A&A*, 382, 368, doi: [10.1051/0004-6361:20011597](https://doi.org/10.1051/0004-6361:20011597)
- Peck, E. R., & Reeder, K. 1972, *Journal of the Optical Society of America* (1917-1983), 62, 958
- Placco, V. M., Sneden, C., Roederer, I. U., et al. 2021, *Research Notes of the American Astronomical Society*, 5, 92, doi: [10.3847/2515-5172/abf651](https://doi.org/10.3847/2515-5172/abf651)
- Placco, V. M., Holmbeck, E. M., Frebel, A., et al. 2017, *ApJ*, 844, 18, doi: [10.3847/1538-4357/aa78ef](https://doi.org/10.3847/1538-4357/aa78ef)
- Planck Collaboration, Ade, P. A. R., Aghanim, N., et al. 2016, *A&A*, 594, A13, doi: [10.1051/0004-6361/201525830](https://doi.org/10.1051/0004-6361/201525830)
- Rix, H.-W., Chandra, V., Andrae, R., et al. 2022, *arXiv e-prints*, arXiv:2209.02722, <https://arxiv.org/abs/2209.02722>
- Roederer, I. U., Kratz, K.-L., Frebel, A., et al. 2009, *ApJ*, 698, 1963, doi: [10.1088/0004-637X/698/2/1963](https://doi.org/10.1088/0004-637X/698/2/1963)
- Roederer, I. U., Sakari, C. M., Placco, V. M., et al. 2018, *ApJ*, 865, 129, doi: [10.3847/1538-4357/aadd92](https://doi.org/10.3847/1538-4357/aadd92)
- Sakari, C. M., Placco, V. M., Farrell, E. M., et al. 2018, *ApJ*, 868, 110, doi: [10.3847/1538-4357/aae9df](https://doi.org/10.3847/1538-4357/aae9df)
- Savard, G., Brodeur, M., Clark, J. A., Knaack, R. A., & Valverde, A. A. 2020, *Nuclear Instruments and Methods in Physics Research B*, 463, 258, doi: [10.1016/j.nimb.2019.05.024](https://doi.org/10.1016/j.nimb.2019.05.024)
- Schatz, H., Toenjes, R., Pfeiffer, B., et al. 2002, *ApJ*, 579, 626, doi: [10.1086/342939](https://doi.org/10.1086/342939)
- Shulyak, D., Ryabchikova, T., Kildiyarova, R., & Kochukhov, O. 2010, *A&A*, 520, A88, doi: [10.1051/0004-6361/200913750](https://doi.org/10.1051/0004-6361/200913750)
- Sneden, C., Cowan, J. J., & Gallino, R. 2008, *ARA&A*, 46, 241, doi: [10.1146/annurev.astro.46.060407.145207](https://doi.org/10.1146/annurev.astro.46.060407.145207)
- Sneden, C. A. 1973, PhD thesis, University of Texas, Austin
- Sobeck, J. S., Kraft, R. P., Sneden, C., et al. 2011, *AJ*, 141, 175, doi: [10.1088/0004-6256/141/6/175](https://doi.org/10.1088/0004-6256/141/6/175)
- Soderblom, D. R. 2010, *ARA&A*, 48, 581, doi: [10.1146/annurev-astro-081309-130806](https://doi.org/10.1146/annurev-astro-081309-130806)
- Tayar, J., Somers, G., Pinsonneault, M. H., et al. 2017, *ApJ*, 840, 17, doi: [10.3847/1538-4357/aa6a1e](https://doi.org/10.3847/1538-4357/aa6a1e)
- Unsöld, A. 1955, *Physik der Sternatmosphären*, MIT besonderer Berücksichtigung der Sonne.
- Valcin, D., Bernal, J. L., Jimenez, R., Verde, L., & Wandelt, B. D. 2020, *JCAP*, 2020, 002, doi: [10.1088/1475-7516/2020/12/002](https://doi.org/10.1088/1475-7516/2020/12/002)
- Valentini, M., Chiappini, C., Bossini, D., et al. 2019, *A&A*, 627, A173, doi: [10.1051/0004-6361/201834081](https://doi.org/10.1051/0004-6361/201834081)
- VandenBerg, D. A., Bond, H. E., Nelan, E. P., et al. 2014, *ApJ*, 792, 110, doi: [10.1088/0004-637X/792/2/110](https://doi.org/10.1088/0004-637X/792/2/110)

Vogt, S. S., Allen, S. L., Bigelow, B. C., et al. 1994, in
Society of Photo-Optical Instrumentation Engineers
(SPIE) Conference Series, Vol. 2198, Instrumentation in
Astronomy VIII, ed. D. L. Crawford & E. R. Craine, 362,
doi: [10.1117/12.176725](https://doi.org/10.1117/12.176725)

Xiang, M., & Rix, H.-W. 2022, *Nature*, 603, 599,
doi: [10.1038/s41586-022-04496-5](https://doi.org/10.1038/s41586-022-04496-5)